Albedo control of seasonal south polar cap recession on Mars

Frédéric Schmidt, Sylvain Douté, Bernard Schmitt, Mathieu Vincendon, Jean-Pierre Bibring, Yves Lanvevin, The Omega Team

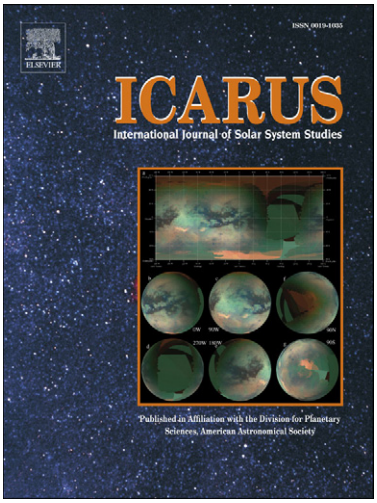

Albedo control of seasonal south polar cap recession on Mars

Frédéric Schmidt, Sylvain Douté, Bernard Schmitt, Mathieu Vincendon, Jean-Pierre Bibring, Yves Lanvevin, the OMEGA Team

PII: S0019-1035(08)00435-1
DOI: 10.1016/j.icarus.2008.12.014
Reference: YICAR 8845

To appear in: *Icarus*

Received date: 19 December 2007
Revised date: 9 October 2008
Accepted date: 1 December 2008

Please cite this article as: F. Schmidt, S. Douté, B. Schmitt, M. Vincendon, J.-P. Bibring, Y. Lanvevin, the OMEGA Team, Albedo control of seasonal south polar cap recession on Mars, *Icarus* (2009), doi: 10.1016/j.icarus.2008.12.014

Albedo Control of Seasonal South Polar Cap Recession on Mars

Frédéric Schmidt [b], Sylvain Douté [a], Bernard Schmitt [a], Mathieu Vincendon [c], Jean-Pierre Bibring [c], Yves Lanvevin [c], and the OMEGA Team

[a] *Laboratoire de Planétologie de Grenoble, Université de Grenoble, CNRS, INSU, BP 53, 38041 Grenoble Cedex 9, France*

[b] *ESA - ESAC, PO Box 78, E-28691 VILLANUEVA DE LA CAÑADA MADRID, Spain*

[c] *Institut d'Astrophysique Spatiale, Université Paris XI, Bâtiment 121, 91405 Orsay cedex, France*

Number of pages: 88
Number of tables: 5
Number of figures: 14

Email addresses: fschmidt@sciops.esa.int (Frédéric Schmidt), sylvain.doute@obs.ujf-grenoble.fr (Sylvain Douté).

Proposed Running Head:
Albedo control SSPC recession

Please send Editorial Correspondence to:

Frédéric Schmidt
ESA - ESAC
PO Box 78
E-28691 VILLANUEVA DE LA CAÑADA MADRID
SPAIN

Email: fschmidt@sciops.esa.int
Phone: (+34) 91 81 31 421
Fax: (+34) 91 81 31 325

ABSTRACT

Over the last few decades, General Circulation Models (GCM) have been used to simulate the current Martian climate. The calibration of these GCMs with the current seasonal cycle is a crucial step in understanding the climate history of Mars. One of the main climatic signals currently used to validate GCMs is the annual atmospheric pressure cycle.

It is difficult to use changes in seasonal deposits on the surface of Mars to calibrate the GCMs given the spectral ambiguities between CO_2 and H_2O ice in the visible range. With the OMEGA imaging spectrometer covering the near infra-red range, it is now possible to monitor both types of ice at a spatial resolution of about 1 km. At global scale, we determine the change with time of the Seasonal South Polar Cap (SSPC) crocus line, defining the edge of CO_2 deposits. This crocus line is not symmetric around the geographic South Pole. At local scale, we introduce the snowdrop distance, describing the local structure of the SSPC edge. Crocus line and snowdrop distance changes can now be used to calibrate GCMs.

The albedo of the seasonal deposits is usually assumed to be a uniform and constant parameter of the GCMs. In this study, albedo is found to be the main parameter controlling the SSPC recession at both global and local scale. Using a defrost mass balance model (referred to as D-frost) that incorporates the effect of shadowing induced by topography, we show that the global SSPC asymmetry in the crocus line is controlled by albedo variations. At local scale, we show that the snowdrop distance is correlated with the albedo variability. Further GCM improvements should take into account these two results.

We propose several possibilities for the origin of the asymmetric albedo control. The next step will be to identify and model the physical processes that create the albedo differences.

Keywords: MARS, SURFACE, MARS, POLAR CAPS, ICE, SPECTROSCOPY

1 Introduction

A significant fraction of the Martian atmosphere, mainly composed of CO_2, is trapped during winter on the planet's surface at high latitudes in the form of CO_2 frost. When the sunlight returns in spring, the frost radiative balance becomes positive and CO_2 sublimates and returns into the atmosphere. This main features of the Martian seasonal cycle were revealed by the pioneering work of Leighton and Murray, 1966.
The OMEGA imaging spectrometer confirmed that the Seasonal South Polar Cap (SSPC) of Mars, during its recession phase, is essentially composed of CO_2 ice. As discussed by Langevin et al., 2007, the H_2O ice signature, detected in the solar longitude range Ls=110°-193°, is probably due to clouds in the atmosphere. Surface H_2O ice is present only at some specific locations over the range of Ls 220°-250°. On the other hand, the Seasonal North Polar Cap involves both H_2O and CO_2 frosts (Schmitt et al., 2006). In this article, we will consider only CO_2 in the SSPC.

During the recession phase, different processes of energy loss/gain are involved in the defrost mass balance, namely latent heat consumption due to CO_2 frost sublimation, thermal emission, absorption of direct and indirect (scattered) sunlight, absorption of thermal emissions from the atmosphere and the surrounding terrain and conduction of thermal energy in the ground. Different parameters are involved in those processes, including albedo as suggested by Piqueux et al., 2003 and Colaprete et al., 2005, thermal emissivity as accurately modeled by Forget et al., 1998, slopes and surface roughness (Veverka and Goguen, 1973; Aharonson and Schorghofer, 2006), thermal inertia of the ground (Aharonson, 2004), annual surface pressure change, altitude and heat advection from the atmosphere.

Recent General Circulation Models (GCMs), integrating processes involved in the CO_2 cycle (including CO_2 snow formation and precipitation), are able to reproduce the Viking Lander 1 pressure measurements (Forget et al., 1998, 1999), assuming a uniform and constant albedo value for the seasonal caps and no surface slope effects. Nevertheless, albedos observed by Viking (James et al., 1979) and more recently by MOC (James et al., 2001; Benson and James, 2005) and TES (Kieffer et al., 2000) and OMEGA (Langevin et al. (2007)) are changing in space and time.
Current GCMs are able to reproduce the time evolution of the surface area covered by CO_2 frost (Lewis et al., 1999). In order to enhance our confidence in both present and past climate studies, the next generation of GCMs should reproduce the latitude of the so called "crocus line" at local scale as a function of longitude and time. For that purpose, they must take into account the changes in time and space of the parameters controlling the processes listed above.

The aim of this article is to determine the relative importance of these factors in controlling SSPC recession.

We will pursue the following objectives:

(1) Monitorthe spatial distribution and albedo of H_2O and CO_2 ices in the SSPC as a function of time using a set of OMEGA observations for the time period ranging from Ls=110° to Ls=320°. For that purpose, we use an automatic detection algorithm called Wavanglet (Schmidt et al., 2007). Concepts describing the structure of the SSPC edge ("inner crocus line", "outer crocus line" and "snowdrop time") are introduced, based on detection statistics inside latitudinal bins. The evolution of the latitude and structure of the SSPC edge as a function of time and longitude constitutes our main constraint. (Section 2).
(2) Model, for an ice layer, the daily and cumulative CO_2 frost mass budget by integrating the radiative gains and losses from or toward space as well as the conductive heat coming from the ground. Special care will be taken in the modeling of the topographically induced shadows. The mass balance is calculated for individual facets with their own altitude and slope orientation based on MOLA DTM. (Section 3)
(3) Perform a sensitivity study of the model regarding to its principal parameters, namely thermal inertia of the ground linked with subsurface heat release, altitude linked with the temperature of the CO_2 layer, surface roughness linked with shadowing effects and thus with absorption of solar light, emissivity linked with thermal emission of the ice (section 4).
(4) Challenge the model with various measurements of the SSPC, including spatial and temporal distributions of the CO_2 ice occurrence as determined by OMEGA (see objective 1), spatial and temporal distributions of the CO_2 ice albedo as measured by OMEGA (see objective 1), total mass accumulation retrieved from neutron flux measurements by GRS and HEND. This analysis is done at two spatial scales:
    (a) global scale (i.e. flat South Polar region divided into two longitude sectors, cryptic and anti-cryptic). We show that the model is compatible with all measurements, using simple analytical laws for the visible and infrared albedo dependence with latitude and time (section 4.1.8),
    (b) local scale (i.e. rough South Polar region, divided into facets at a resolution of 1 km). We demonstrate that the structure of the SSPC edge cannot be predicted by the model using the smooth albedo variation already used at global scale. We found a correlation between the structure of the SSPC edge and the distribution of albedo observed by OMEGA at the location of the transition zone, but more than 10 Martian days before its passage (section 4.2).
(5) Discussion of the processes that potentially govern the albedo global asymmetry between the cryptic and anti-cryptic sectors and that can

explain the albedo variability at the lower spatial scale (Section 5).

2 Analyzing a sequence of OMEGA/MEX observations for monitoring CO_2 and H_2O ices

The aim of this section is to present how we monitor the SSPC during the recession phase, when ice sublimates.

2.1 Selection of OMEGA observations

The imaging spectrometer OMEGA on board Mars Express has acquired the most comprehensive set of observations to date in the near-infrared (0.93-5.1 microns) on the SSPC from winter solstice to the end of the recession at Ls=325° (Langevin et al., 2007). Monitoring the spatial distribution of CO_2 and H_2O ice requires their automatic detection due to the large number of images. For that purpose, we developed a method called "Wavanglet" (Schmidt et al., 2007) that is described briefly in the next section.

From Ls=110° to Ls =320° of Martian year 27 (early 2005 to mid 2006), we select a total of 605 OMEGA/MEX observations with a positive detection of CO_2 ice at high southern latitudes.

2.2 Wavanglet detection method

The detection is carried out by comparing each spectrum of an image with reference spectra of compounds we want to detect in an optimized subspace of wavelets. The correlation between the reduced observed and reference spectra is calculated and compared to a threshold in order to declare detection (1) or absence (0). After the processing of an OMEGA image, the Wavanglet algorithm provides one binary image with the same spatial dimensions - called the *detection mask* - for each reference compound (Schmidt et al., 2007).

We take into account the information about corrupted spectels and lines and we systematically remove spectra acquired with incidence angles higher than 85° and/or emergence angles higher than 70° (low signal to noise ratio). In this study we use four references, namely one synthetic (i.e. generated by a radiative transfer model) spectrum of CO_2 ice, one synthetic spectrum of H_2O ice, one endmember spectrum of dust extracted from an OMEGA image and one endmember spectrum of water ice clouds observed over Hellas.

2.3 Position and structure of the polar cap edge

Previous studies on the south seasonal cap recession in the visible range have been completed by several authors (James et al., 1979; Iwasaki et al., 1990; James et al., 2000; Benson and James, 2005). Other studies in the infrared range were conducted by Kieffer et al. (2000) using the TES instrument. These authors consider that a sudden rise of surface temperature, from around 145 K (the temperature of CO_2 ice in equilibrium with the atmosphere) to about 230 K (the temperature of the mineral bare ground) indicates the passage of the sublimation front. For a given location, fitting the temporal evolution of the temperature by an arctangent empirical law provides the crocus date which, by definition, coincides with the inflection of the curve. The crocus line is the set of locations, where the crocus dates are equal to a given Ls. In the visible range, another specific law is used to parametrize the decrease of albedo and evaluate the crocus date, assuming such event coincides with CO_2 disappearance. These studies already suggested that the edge of the seasonal cap is a transition zone where patches of CO_2 ice and dust coexist geographically over a certain spatial extent.

In this article, we propose to characterize the transition zone by defining "inner and outer crocus lines" using CO_2 detection by OMEGA in the near infrared. We define a *bin,* an element 0.3° by 10°, respectively in latitude and longitude, belonging to a geographical grid. Hundreds of OMEGA pixels usually fall into such a bin making it possible to calculate statistics for different physical quantities. A *meridian profile* is the latitude sequence of values calculated for the bins falling into the same longitude range (see appendix A).

@@@@@ FIGURE 1

First we segment all CO_2 detection masks (see previous section) into bins. The OMEGA spatial resolution can change from 2 km to 700 m depending on observation conditions but the bin size is constant. The same grid is used to represent the model results (see appendix A for definition of scales). For each bin, the CO_2 *ice coverage* indicator f_{CO_2} is the number of pixels with positive detection of CO_2 divided by the total number of pixels. In case of sub-pixel mixing, f_{CO_2} is an approximation of the real coverage.

Second, we build a meridian profile of CO_2 ice coverage for each individual OMEGA image corresponding to a given Ls. The bins that contain a border (border of the observation, border of corrupted portions of an image) are eliminated in order to prevent biases.

@@@@ FIGURE 2

Third, from each meridian profile, we extract the inner/outer limits of the

SSPC according to 3 rules:

- outer crocus line, i.e. the bin that contains a CO_2 ice coverage f_{CO_2} higher than 1% and that is the closest to the equator,
- inner crocus line, i.e. the bin that contains a CO_2 ice coverage f_{CO_2} lower than 99% and that is the closest to the pole,
- inner and outer crocus line, i.e. the bin that contains the inner/outer crocus line is valid only if its adjacent neighbor bins contain no image border.

When treating our selection of OMEGA images, we determine the latitude of both crocus lines at discrete values of Ls (time) for 36 intervals 10° wide in longitude. At a given location, following the definition by Kieffer et al., 2000, we propose to name the date when the inner crocus line (respectively outer crocus line) crosses that location the "inner crocus date" (respectively the "outer crocus date").

The latitudinal distance (resp. temporal gap) between the inner and outer crocus lines (resp. crocus date), that defines the width (resp. time) of the CO_2 snow drop, can be named SNOW-DROP. Incidentally, the term "snowdrop" also denotes a flower that grows through snow in spring on Earth. For convenience, and because we prefer flowers to inelegant acronyms, we propose the more simple term "snowdrop" (see Fig. 1).

At global scale, the position of the SSPC observed by OMEGA, described by the mean crocus line, is usually not symmetric around the geographic South Pole. At local scale, the structure of the SSPC edge, described by the snowdrop time, changes with time/latitude and longitude. The mean value of the snowdrop time is 15°Ls, but it can vary from a few degrees up to more than 30°Ls. In some extreme situations, the snowdrop time can reach half of the total sublimation duration showing that this transition period can be very long. One goal of this paper is to understand these patterns and link them to processes and physical parameters.

2.4 Monitoring the albedo with OMEGA

Calculating the instantaneous or integrated mass budget requires monitoring of the ice bolometric albedo, under the aerosols layer. Definition of the bolometric albedo $A_{dh,vis}$, spectrally integrated (weighted by the solar spectrum) and directional-hemispheric (dependent on the incidence direction and integrated on all emergence directions of the upper hemisphere) can be found in Hapke, 1993.

Practically speaking, accurate evaluation requires either consecutive (Paige and Ingersoll, 1985) or simultaneous (for instance with the CRISM instrument

by Murchie and and 42 colleagues, 2004) multi-angular sampling of the bidirectional reflectance distribution function (BRDF) of the icy terrain. Multi-angular OMEGA data (EPF) that would allow us to constrain the BRDF prior to directional integration are very sparse in space and time. As a consequence, monitoring the bolometric albedo of the entire SSPC from OMEGA images lies outsidethe scope of this paper. We will suppose that the surface is lambertian.

For quantitative studies at global scale (see section 4.1), we propose to estimate the bolometric albedo, noted A^B_{vis}, in a two step process. First, estimation of the CO_2 ice reflectance $R^V_{1.07}(\theta_i, \theta_e, \theta_a)$ at 1.07 microns in the continuum using Vincendon's approach to remove the contribution of aerosols (Vincendon et al., 2008). The use of this spectral channel was also proposed by Langevin et al., 2007 who argues that it combines a high signal to noise ratio, high radiometric accuracy and no absorption bands due to CO_2 ice, H_2O ice and CO_2 gas. We can note that, after Ls=220°, water ice clouds are completely absent in the South Polar region. At 1.07 microns, dust aerosols significantly modify the apparent surface albedo, notably for bright icy surfaces which appear darker. Vincendon's method evaluates the contribution of the aerosol scattering and attenuation at all wavelengths from a narrow spectral region where the entire signal comes from the aerosols (saturated bands of CO_2 ice). Second, estimation of the spectrally integrated albedo from the reflectance $R^V_{1.07}(\theta_i, \theta_e, \theta_a)$ using an empirical law (see fig. 3). Indeed we found a linear relationship between A_{vis} and $R_{1.07}$, on the one hand, by weighting and integrating the OMEGA visible and near IR channels and, on the other, using the lambertian hypothesis. As a first approximation, we suppose that the aerosol contribution always has the same spectral shape, such that the linear relationship is always valid. For global scale, the final relation is:

$$A_{dh,vis}(\theta_i) \simeq A^B_{vis} = 0.812 \times R^V_{1.07}(\theta_i, \theta_e, \theta_a) + 0.009 \quad (1)$$

For albedo studies at local scale (see section 4.2), it is not possible to use Vincendon's method to estimate the aerosol contribution everywhere because the CO_2 ice absorption bands are not always saturated. As a crude approximation, we will use instead the reflectance $R^O_{1.07}$ measured by OMEGA in the continuum at 1.07 microns for a combination of incidence and emergence angles that vary weakly from pixel to pixel. We will assume that the local maximum of albedo variability, if constant over a long period of time, is more likely to be at the surface rather than in the atmosphere. For local scale, the final relation is:

$$A_{dh,vis}(\theta_i) \simeq A^O_{vis} = 0.812 \times R^O_{1.07}(\theta_i, \theta_e, \theta_a) + 0.009 \quad (2)$$

with θ_i the incidence angle, θ_e the emergence angle, and θ_a the azimuth.

@@@@ FIGURE 3

In this study, we calculate the average and the variance of the "albedo" in each bin of the grid based on the pixels with positive detection of CO_2 (see Appendix A for definition of scales). Such quantity will be denoted A^B_{vis} and A^O_{vis}.

3 D-frost, the daily and cumulative CO_2 frost mass budget model

The aim of this section is to introduce the D-frost mass balance model used to solve the equations of a terrain facet (defined by location and slope) that is already covered by a layer of CO_2 ice.

3.1 Topography and roughness measured by MOLA

The MOLA topographic dataset covers the South Polar region at a resolution of 1/64 degree (available on line [1]). The dataset is interpolated where no data is recorded, especially near the geographic South Pole from latitude 90°S to 86°S. We use a map built according to a South Polar stereographic projection and a resolution of 920 m, comparable to the best OMEGA spatial resolution (≈700 m). Better spatial resolution is available but, in this case, the calculation time of our model would be too long (in excess of one month). We define each pixel of the MOLA dataset as a facet (see Appendix A for definition of scales).

MOLA topography We calculate the local slope as a function of the geographic coordinates by differentiating the MOLA topography $h(x, y)$ with the following operator:

$$\begin{cases} \frac{\partial}{\partial L} = \frac{2R\cos(\phi)}{1-\sin(\phi)}\left(-\sin(L)\frac{\partial}{\partial y} + \cos(L)\frac{\partial}{\partial x}\right) \\ \frac{\partial}{\partial \phi} = \frac{2R}{1-\sin(\phi)}\left(\cos(L)\frac{\partial}{\partial y} + \sin(L)\frac{\partial}{\partial x}\right) \end{cases} \quad (3)$$

L being the east increasing longitude, ϕ the latitude, R the radius of the planet and (x, y) the map coordinates. In order to retrieve a dimensionless slope, the altitude is expressed in radian $h' = \frac{h}{R}$ and the derivatives are estimated by $\frac{\partial}{\partial x}h(x_i, y_i) = \frac{h'(x_{i+1},y_i)-h'(x_i,y_i)}{(x_{i+1}-x_i)} = \frac{h(x_{i+1},y_i)-h(x_i,y_i)}{R.(x_{i+1}-x_i)}$.

[1] http://pds-geosciences.wustl.edu/missions/mgs/megdr.html

This method has the advantage of producing a result for all points in this projection. Nevertheless, the errors due to the map projection and to the interpolation of several MOLA points are difficult to estimate.

MOLA roughness Surface roughness is defined relatively to all scales higher than the facet size. Several statistical descriptors of this quantity can be found in the literature (Shepard et al., 2001; Aharonson et al., 2001), namely the standard deviation of the altitude $h(x, y)$ from the mean or more robustly from the median, interquartiles and the decorrelation length. Pioneer work on roughness as an instance of fractal distribution was done by Sayles and Thomas, 1978. Such description was applied for the north polar cap using MOLA data by Malamud and Turcotte, 2001. They used wavelets to estimate roughness as the local value of the power law dependence of the power spectral density on frequency. They estimated the exponent $\beta \simeq 3.5$ for the south permanent cap and $\beta \simeq 2$ for the surrounding terrain. An alternative theory describes roughness as the local value of the exponent of the RMS slope as a function of baseline, i.e. the Hurst exponent H. Recently Aharonson and Schorghofer, 2006 estimated a local value of H which is about 0.8 for both Mars as a whole and the region occupied by the seasonal South Polar cap. In this study, we use the Hurst exponent fractal description of the roughness because an adapted model of a self-shadowing function is provided by Shepard and Campbell, 1998.

The study by Campbell et al., 2003 suggests that the MOLA dataset cannot be extrapolated for roughness scales lower than 15 m. In addition, no datasets are available for the complete South Polar region of Mars. In this article, the roughness at scales below the facet size are ignored.

3.2 Daily averaged radiation absorbed by frost

Computing the seasonal radiation budget is an important step in understanding the climate of the polar regions. From the parametrization of the "instantaneous" absorbed energy Q by Kieffer et al., 1977; Schorghofer and Aharonson, 2005; Aharonson and Schorghofer, 2006, we will compute the daily averaged absorbed radiation W at a given location on the surface of Mars using the integration method used by (Laskar et al., 1993). There are four sources, namely direct sunlight Q_{sun}, sunlight scattered by the atmosphere Q_{scat}, thermal emission by the atmosphere Q_{IR} and thermal emission by the neighboring facets Q_{floor}.

$$W = \int (Q_{sun} + Q_{scat} + Q_{IR} + Q_{floor})\, dt \tag{4}$$

All these terms depend on local slope γ. We will use the following notation for three normalized vectors, that is $\overrightarrow{r_{surf}}(L,\phi)$for the radius vector pointing at a location on the surface assuming a spherical planet, $\overrightarrow{r_{sun}}(\alpha,\delta)$for the radius vector of the sub-solar point and $\overrightarrow{n_{surf}}(L_n,\phi_n)$for the direction normal to the local surface. The coordinates are expressed in increasing east longitude (L, α, L_n are from 0 to 2π) and latitude (ϕ, δ, ϕ_n are from $-\frac{\pi}{2}$ to $\frac{\pi}{2}$). The local slope γ is defined as:

$$\gamma = \arctan\sqrt{\left(\frac{\partial topo}{\partial \phi}\right)^2 + \left(\frac{\partial topo}{\partial L}\right)^2} \quad (5)$$

In order to simplify the equation, the integration of the "instantaneous" insolation is performed relative to longitude L instead of time as in Laskar et al. (1993), assuming that the relative orientation of the planet rotation axis and the sun direction is constant during a day, which is a reasonable assumption for planet Mars. The integration method is described in appendix B.

Integration of the different contributions Q_{sun}, Q_{scat}, Q_{IR} and Q_{floor} are explicitly described below.

(1) Direct solar illumination

$$Q_{sun} = \frac{S_{sun}}{r_{sun}^2}(1-f)^{1/\max\left((\overrightarrow{r_{surf}}\bullet\overrightarrow{r_{sun}}),0.04\right)}(1-A_{vis})(\overrightarrow{n_{surf}}\bullet\overrightarrow{r_{sun}})\Psi(\overrightarrow{r_{surf}}\bullet\overrightarrow{r_{sun}},H,\gamma) \quad (6)$$

The first ratio is the solar constant at the heliocentric distance of Mars, the second factor expresses the absorption of radiation by the surface, the third represents the parametrized atmospheric attenuation (Kieffer et al., 1977; Schorghofer and Aharonson, 2005; Aharonson and Schorghofer, 2006), the fourth term expresses the geometrical effect and the fifth term Ψ quantifies the loss of illumination due to self-shadowing effects linked with roughness. In the following, these five factors will be noted F_1 to F_5. We use the empirical shadowing function for fractal surfaces $\Psi(\overrightarrow{r_{surf}}\bullet\overrightarrow{r_{sun}},H,\gamma)$, truncated to the 6th term, determined by Shepard and Campbell, 1998:

$$\Psi(\overrightarrow{r_{surf}}\bullet\overrightarrow{r_{sun}},H,\gamma) = 1-\frac{1}{2}\sum_{n=1}^{6}\frac{1}{2.3^{n-1}}erfc\left(\frac{n^{1-H}}{\sqrt{2}\frac{\sqrt{1-\left(\overrightarrow{r_{surf}}\bullet\overrightarrow{r_{sun}}\right)^2}}{\left(\overrightarrow{r_{surf}}\bullet\overrightarrow{r_{sun}}\right)}\tan(\gamma)}\right) \quad (7)$$

We estimate the integral quantities using a Simpson numerical integration scheme (Press et al., 1986-1992).

(2) Indirect solar illumination by scattering in the atmosphere (half of the scattering lost in space) and absorbed by the surface according to Kieffer et al., 1977 and Aharonson and Schorghofer, 2006:

$$Q_{scat} = \frac{S_{sun}}{r_{sun}^2} f_{scat} \frac{1}{2} (1 - A_{vis}) \cos^2(\frac{\gamma}{2}) \tag{8}$$

(3) Surface heating by thermal emission of the atmosphere according to Kieffer et al., 1977 and Aharonson and Schorghofer, 2006:

$$Q_{IR} = \frac{S_{sun}}{r_{sun}^2} f_{IR} (1 - A_{IR}) \cos^2(\frac{\gamma}{2}) \, (\overrightarrow{r_{surf}} \bullet \overrightarrow{r_{sun}})_{noon} \tag{9}$$

The cosine of the incidence angle at noon for a flat surface: $(\overrightarrow{r_{surf}} \bullet \overrightarrow{r_{sun}})_{noon}$

$$(\overrightarrow{r_{surf}} \bullet \overrightarrow{r_{sun}})_{noon} = (\overrightarrow{r_{surf}} \bullet \overrightarrow{r_{sun}})_{L=\alpha} = \sin(\frac{\pi}{2} + \phi - \delta) \tag{10}$$

(4) Surface heating by thermal emission of the surrounding soil, as in Kieffer et al., 1977 and Aharonson and Schorghofer, 2006:

$$Q_{floor} = \varepsilon \sigma T^4 (1 - A_{IR}) \sin^2(\frac{\gamma}{2}) \tag{11}$$

The parameter values used for the surface radiation budget are summarized in appendix C.

3.3 Daily and cumulative defrost mass balance

3.3.1 Estimation of the "instantaneous" CO_2 defrost balance

We estimate the instantaneous CO_2 frost mass balance using the energy balance at the surface. We compute the daily radiation budget and neglect the heat advection from the atmosphere, which is a correct hypothesis for the sublimation phase as suggested by GCM studies (Forget, 1998). The flux of mass resulting from the energy balance is:

$$\frac{\partial M_{CO_2}}{\partial t} = (F_{therm}^{out} - W_{sun}^{in} - W_{scat}^{in} - W_{IR}^{in} - W_{floor}^{in} - F_{cond}^{in}) \frac{1}{L_{CO_2}} \tag{12}$$

This equation can also be used for the daily balance assuming that the albedo and surface temperature of the facet do not change within the course of a day. A possible recondensation of CO_2 during the night on bare ground during the SSPC recession is not taken into account in this modeling. We neglect heat diffusion within the frost deposits by absorption and release of latent heat due to sublimation/recondensation and gas diffusion. We assume no metamorphism.

The different contributions of Eq. 12 are described below.

(1) Energy loss is the outgoing thermal flux from CO_2 frost at the surface. This term is estimated by a gray body emission as proposed by Warren et al., 1990:

$$F_{therm}^{out} = \varepsilon \sigma T_{surf}^4 \tag{13}$$

Surface temperature T_{surf} is determined assuming that CO_2 frost at the surface is in equilibrium with atmospheric CO_2 gas at surface pressure P_{surf}. We use the surface pressure calculated by the GCM of Forget et al., 1999 for a given date (season), location and altitude. This estimation takes into account the annual pressure cycle measured by Viking.
We use the empirical parametrized saturation curve proposed by Brown and Ziegler, 1979 to convert P_{surf} into temperature T_{surf}. This method is correct only when CO_2 frost is already present on the facet.

(2) Energy gain is the absorbed radiative flux:

$$-W_{sun}^{in} - W_{scat}^{in} - W_{IR}^{in} - W_{floor}^{in} \tag{14}$$

Those terms are estimated according to the method described in the section 3.2 (Eq. 4).

(3) Energy gain is the conducted internal heat flux from planet Mars. It has two different origins.
   (a) Annual heat wave in the ground. This term can be neglected during the recession phase, as demonstrated in section 4.1.3.
   (b) Geothermal heat flux. There is no direct measurement of the heat flux from planet Mars but several authors estimated it to be between 15 and 45 mW m^{-2} on average (Shchuko et al., 2003). For comparison, on Earth the average value is around 80 mW m^{-2}. We assume that it is spatially and temporally constant:

$$F_{cond}^{in} = 40 \,\text{mW m}^{-2} \tag{15}$$

The order of magnitude of this flux is generally negligible in the cumulative frost balance when compared with the other terms. Nevertheless, for facets in the shadow, it could accelerate the occurrence of the crocus date by typically one Martian day.

3.3.2 Cumulative mass loss during recession

We can estimate the cumulative mass loss of frost during the SSPC recession by integrating the "instantaneous" frost mass balance. We perform the integration between 2 dates T_{beg}^M and T_{end}^Mexpressed in solar longitude Ls with a time step of 5°. We start the calculation at Ls=90°. The integration begins when the

balance becomes negative, at a date noted T^M_{beg} (beginning of the recession as determined by the model M) that is, when the seasonal polar cap begins to sublimate. The date T^M_{beg} depends mainly on latitude, albedo and slope. T^M_{end} is the "mean" crocus date, the date of the end of the sublimation, T^M_{end}.

To convert Julian time expressed in seconds into time expressed in °Ls , we use the J2000 relations which can be found in Allison and McEwen, 2000.

The parameters used for modeling the defrost mass balance are summarized in appendix D.

3.4 Latitudinal profiles of W and M_{CO_2}

We perform the calculation of the absorbed radiation W and of the frost mass balance M_{CO_2} for all the facets of the MOLA grid expressed in stereographic south projection. In order to compare both modeled and observed crocus lines, we arrange the facets inside the set of bins described in section 2.4. For each bin, we calculate the mean and the variance of W and M_{CO_2}, both based on the population of facets within the bin. We present the results in the form of meridian profiles (see section 2.3).

Both daily absorbed radiation and defrost mass are estimated every 5°Ls (almost 10 Martian days). This time sampling interval is a compromise between accuracy and computational time (1 month for the M_{CO_2} on a bi-processor AMD Opteron 250, 64 bits, 2.4 Ghz).

4 Results

At global scale, we show that the asymmetry of the SSPC crocus line is a consequence of a pre-existing asymmetry of the visible albedo. For both the cryptic and anti-cryptic sectors, we find that our sublimation model is compatible with the net accumulation measurements by HEND and GRS, as well as with the crocus line and albedo determined by OMEGA. At local scale, the SSPC snowdrop distance is controlled by the state of albedo distribution more than 5°Ls before the crossing of the inner crocus line.

We performed a sensitivity study that demonstrates that during the recession phase, the following effects/parameters have limited effects on CO_2 stability, namely heat exchange with the ground, altitude, surface roughness (slope and shadow), emissivity and albedo in the thermal infrared.

The high resolution accumulation field is difficult to estimate accurately be-

cause the only available measurements come from instruments with low spatial resolution. In addition, no accurate modeling of the SSPC CO_2 sublimation at such small scales is currently available (neither the temporal and spatial albedo variation, nor the effect of slope have been incorporated in the model). We assume in our calculations that the net accumulation has a smooth latitudinal dependency.

4.1 Recession at global scale

The global SSPC recession is not symmetric around the geographic South Pole as previously observed by Viking (James et al., 1979). Using TES data, Kieffer et al., 2000 define the *cryptic region* where CO_2 ice (at low temperature) has a low albedo. As seen in Fig. 4, this region recesses faster. This asymmetry is also observed with OMEGA data as mentioned by Langevin et al., 2007. We define the cryptic sector between longitude 60°E and 260°E, the anti-cryptic sector being the complementary, i.e. between longitude 100°W and 60°E.
In order to roughly describe the asymmetry, we estimate the mean OMEGA crocus line (or simply crocus line) for both sectors. We take the middle line between the inner and the outer crocus lines (Fig. 2) to ensure coherence with the definition by Kieffer et al., 2000. The crocus date can be noted T^O_{end}, as the date of the end of the recession observed by OMEGA. We estimate the crocus date for 4 latitudes that are also considered in a HEND study by Litvak et al., 2007. At latitude 65°S, the typical crocus date is Ls=220° for the cryptic sector and Ls=225° for the anti-cryptic sector. At latitude 85°S, the difference goes up to 20°Ls.
In the cryptic sector, some seemingly defrosted points (outliers) are present at latitudes higher than 70°S in the time period from Ls=180° to Ls=230° (Fig. 4). This is due to the fact that some CO_2 deposits of the cryptic sector are covered by an optically thick mantle of dust as suggested by Langevin et al., 2006.

@@@@ FIGURE 4

The near infrared view by OMEGA differs from the one offered by TES in the thermal infrared at 30 microns (see Fig. 4). The OMEGA crocus lines are at significantly lower latitudes compared to TES, even outside the interannual variability measured by TES for Martian years 25, 26 and 27. This fact is probably due to subpixel mixing of ice and dust near the seasonal cap edge. The thermal infrared range is more sensitive to dust than the near infrared, according to the non-linearity of the thermal flux. In addition, the fact that the OMEGA inner crocus line is similar to the TES crocus line evolution suggests that the linear mixing occurs at a scale lower than OMEGA spatial resolution. An accurate comparison between different datasets is lies outside the scope of

this paper, but would be interesting work in the future.

Now we discuss the origin of the SSPC recession asymmetry which we illustrate by two representative meridian profiles, (a) within the cryptic sector (140°-150°E) and (b) within the anti-cryptic sector (270°-280E).
For that purpose, we performed a sensitivity study of the defrost model, relative to the following effects/parameters on $\frac{\partial M_{CO_2}}{\partial t}$, namely annual heat wave in the ground, altitude, surface roughness, albedo and emissivity in the IR and finally albedo in the visible. We also discuss the degree of spatial asymmetry of accumulation $M_{CO_2/tot}$ and the date of the beginning of sublimation T_{beg} as well as of the previous parameters.

4.1.1 CO_2 *ice accumulation* $M_{CO_2/tot}$

From a theoretical point of view, according to Forget, 1998, the mass balance during the net accumulation phase is governed by this equation:

$$\frac{\partial M_{CO_2}}{\partial t} = (F^{out}_{therm} - F^{in}_{adv} - F^{in}_{cond} - W^{in}_{sun} - W^{in}_{scat} - W^{in}_{IR} - W^{in}_{floor})\frac{1}{L_{CO_2}} \quad (16)$$

The term F^{out}_{therm} represents the thermal flux (eq 13). It depends on emissivity ε and altitude via the CO_2 temperature. During the polar night, ε is estimated by $1 - BD_{25}$ with TES measurements by Eluszkiewicz and Moncet, 2003. Before Ls=140°, at latitude 87°S, they estimate that emissivity is around 0.9 for the cryptic sector and 0.75 for the anti-cryptic sector, leading to a lower accumulation mass in the latter. This difference in accumulation is in apparent contradiction with a longer recession time for the anti-cryptic sector. Section 4.1.4 shows that altitude can be considered as symmetric around the South Pole and thus the same is true for the equilibrium temperature.
Equation 16 is slightly different from Eq. 12 that expressed the defrost mass balance. The additional term F^{in}_{adv} represents the heating due to internal, potential and kinetic energy advected by atmospheric motion. Pollack et al., 1990 shows that this term is no longer negligible because it can reach 40 W m^{-2} near the cap edge. This heating can be asymmetric due to the topographic forcing of Hellas and Argyre (Colaprete et al., 2005).
Moreover, the annual heat wave contribution F^{in}_{cond} becomes one of the dominant sources of energy (Aharonson, 2004). On average, for the average SSPC, this term was estimated by Paige and Ingersoll, 1985 to be up to 20-30 W m^{-2}.
An asymmetrical thermal inertia of the subsurface would lead to an asymmetrical accumulation. However, thermal inertia observed by TES is symmetrical around the pole (Putzig et al., 2005).
All radiation terms W are negligible because the main accumulation phase occurs during night time.

From an observational point of view, Viking, TES and OMEGA have observed that the SSPC is symmetric around the pole before Ls=220° at the end of the net accumulation phase (James et al., 1979; Kieffer et al., 2000; Langevin et al., 2007). Moreover a study by Aharonson et al., 2004 using MOLA data reveals that the amplitude of the semi-annual cycle of elevation of the deposits shows no clear asymmetry in the accumulation phase. The HEND (Litvak et al., 2007) and the GRS (Kelly et al., 2006) instruments do not have enough spatial resolution to measure several meridian profiles of accumulation according to longitude.

We conclude that accumulation is likely symmetrical around the geographic South Pole.

4.1.2 Date of the beginning of sublimation T_{beg}

From a theoretical point of view, T_{beg} is the date when the balance expressed by the right hand side of Eq. 16 equals 0. Thus the asymmetry of T_{beg} depends on the asymmetry of all terms. The first three terms were previously discussed in the last section.
The radiation terms W are no longer negligible and will be discussed in sections 4.1.5 to 4.1.7. The most likely parameter that can be asymmetric is the albedo, but the measurement by TES shows that albedo is symmetric from Ls=175 to Ls=200° (Piqueux et al., 2003).

The date T_{beg} is difficult to evaluate by observation. The only direct measurement is by the HEND (Litvak et al., 2007) and the GRS (Kelly et al., 2006) instruments which do not have enough spatial resolution to measure T_{beg} as a function of longitude. Indirect measurement of altitude using MOLA data shows (Aharonson et al., 2004) no clear asymmetry.

Following the same argumentation as in the last section, we conclude that the date of the beginning of sublimation T_{beg} is likely symmetrical around the geographic South Pole. In the next models, T_{beg}will be a free parameter, fixed by the model itself.

4.1.3 Annual heat wave in the ground

As suggested by Aharonson, 2004, the excess of heat absorbed by the ground during summer is partially released in winter. The amount of heat involved in this annual wave depends on the thermal inertia of the subsurface. We use the LMD 1D model (model M1), developed by Forget et al., 1999, to estimate the amount of energy that comes from the ground during the recession phase. We consider the cryptic and anti-cryptic sectors at four latitude points, 55°S, 65°S, 75°S and 85°S. Following the study by Aharonson, 2004, the parameters

of the bare soil are albedo $A_{vis} = 0.29$, emissivity $\epsilon = 0.99$. In the visible, the albedo of the frost is set to the equivalent albedo in the time independent scenario, model M2 (see section 4.1.8). We compute the subsurface heat released during the net sublimation phase for two extreme thermal inertia values, 20 and 1000 J m^{-2} s$^{-1/2}$ K^{-1}, compatible with the range of apparent thermal inertia estimated for the South Polar region determined by Putzig et al., 2005. The integration is conducted from the $T^H_{beg}(L', \phi)$ date of the beginning of net sublimation as measured by HEND to $T^{M1}_{end}(L', \phi)$, the date of the total sublimation of the CO_2 ice layer computed by model M1. We run the model over three consecutive Martian years to make it insensitive to the initial conditions. Subsurface heat is converted to an equivalent sublimated CO_2 mass.
The results are displayed in Tab. 4 for the cryptic sector and in Tab. 5 for the anti-cryptic sector. At maximum, 6% of the total mass sublimated is due to subsurface heat (at latitude 55°S), leading to a shift of the crocus date of less than 2°Ls. For comparison, the difference in crocus dates between the cryptic and anti-cryptic sectors is about 20°Ls.

In conclusion, this source of energy can be neglected in all calculations concerning the recession phase. Nevertheless, subsurface heat is one of the most important sources of energy during the polar night.

4.1.4 Altitude

@@@@ FIGURE 5

Topography around the pole is quasi symmetric (Fig. 5). The maximum altitude difference between the anti-cryptic (orange-red profiles) and cryptic (blue-green profiles) sectors is $\approx$ 1000 m at latitudes higher than 84°S. Two particular regions depart from the general trend at latitudes lower that 60°S, namely the Hellas basin (between 40°E and 90°E) with a minimum altitude of less than -6000 m and the Argyre basin (between 300°E and 330°E) with a minimum altitude of -3000 m. Table 1 summarizes the reference altitude profiles taken for the model.

@@@ TABLE 1

A difference in altitude produces a difference in equilibrium temperature that, in turns, leads to a difference in thermal emission and thus in defrost mass balance. We solve the equation of energy balance at the surface (see section 3.3.1) for the cryptic and anti-cryptic sectors at four latitude points, 55°S, 65°S, 75°S and 85°S. We use the empirical law of time independent but latitude dependent albedo (model M2) as discussed in section 4.1.8. Emissivity is set to 0.99 in order to maximize the effect of altitude on the defrost mass.
At latitude 55°S (Tab. 2), a difference of $\pm$ 1000 m in altitude leads to a difference in defrost mass of $\pm$ 7 kg m^{-2} ($\pm$ 4.4% of the total mass sublimated

during the recession phase) and thus a shift of the crocus date of ± 1°Ls. At 85°S, the difference in defrost mass represents ± 12 kg m^{-2} , i.e. ± 1.1% of the total mass, and thus a shift of the crocus date of ± 0.6°Ls (Tab. 3). For comparison, the observed difference in crocus dates, which is about 20° of Ls at 85°S, corresponds to a defrost mass of 300 kg m^{-2}.

@@@ TABLE 2

@@@ TABLE 3

In conclusion, the small altitude differences of ≈ 1000 m between the cryptic and anti-cryptic sectors cannot explain the SSPC recession asymmetry.

4.1.5 Radiation on a rough surface

This section presents a sensitivity study of our model regarding surface roughness. In order to estimate the effect of slope and shadow induced by surface roughness on the daily average absorbed radiation W (Eq. 4), we compute it using the parametrization presented in section 3.2. We choose the following configuration, $A_{vis} = 0$, $A_{IR} = 0.01$ and $\varepsilon = 0.99$ to maximize the effect of slope and shadow.

Figure 6 represents the meridian profiles of W as a function of Ls for the cryptic and anti-cryptic ranges of longitudes. One can see that the spatio-temporal pattern of W is nearly identical for both sectors despite the fact that the distribution of the facets orientation as well as the roughness of the terrain could be different. This suggests that these factors do not play a role at a first order in the asymmetry.

@@@@ FIGURE 6

4.1.6 Emissivity and albedo in the thermal infra-red

Emissivity and albedo are linked through the Kirchhoff law:

$$A_{IR}(\theta, \lambda) = 1 - \varepsilon(\theta, \lambda) \tag{17}$$

with θ the zenith angle and λ the wavelength. The directional hemispheric albedo for a beam of light with incidence θ is noted $A_{IR}(\theta, \lambda)$. The emissivity at the emergence angle θ is noted $\varepsilon(\theta, \lambda)$.

Neither the emissivity nor the albedo of the surface of Mars in the thermal infrared can be directly measured from space because of ambiguities with

temperatures. Nevertheless, some estimation of emissivity with TES measurements using a band ratio of $\varepsilon = 1 - BD_{25}$ has been done by Eluszkiewicz and Moncet, 2003. This study shows that, during the first year covered by MGS (Martian year 25), the emissivity remains at levels higher than 0.9 for the polar region after Ls=140°. A small asymmetry in emissivity is apparent at this date and then tends to disappear.

Theoretical studies or laboratory measurements provide some other clues. Warren et al., 1990 and more recently Hansen, 1999 propose to model CO_2 ice spectral emissivity using the Mie theory applying the delta-Eddington approximation and using laboratory measured optical constants. In the first study Warren et al., 1990, emissivity is weighted by the Planck function for a temperature of 148K, representative of the SSPC CO_2 frost temperature and averaged from 6 to 25 microns. This spectral domain contains only half of the black body energy, but no optical constants were available at wavelengths longer than 25 microns. For pure CO_2 ice, the emissivity increases with grain size, ranging from 0.29, for a grain size of 5 microns, to 0.91, for 2000 microns. As discussed by Langevin et al., 2007, the grain size of SSPC CO_2 observed by OMEGA ranges from a few millimeters to several dozens of centimeters, leading to an emissivity higher than 0.91. Warren et al., 1990; Hansen, 1999 also shows that the presence of dust and water ice increase the emissivity. Local variability of grain size, water ice and dust content can lead to differences in emissivity from 0.91 (pure CO_2 ice with grain size of 2 mm) to 1.0 (maximum value).

We will use the range of emissivity from 0.91 to 0.99 in agreement with both TES measurements and theoretical considerations.

To estimate accurately the effect of emissivity, we simulate the cumulative frost sublimation mass, by solving the equation of energy balance at the surface (see section 3.3.1) for the anti-cryptic sector at two extreme altitudes and latitude. At 85°S, the cumulative defrosted mass with $\varepsilon = 0.99$ (resp. $\varepsilon = 0.91$) is 1213 kg m^{-2} (resp. 1242 kg m^{-2}). This difference represents 1.6% of the total mass sublimated during the recession phase and accelerates the crocus date by a shift of -1.6°Ls. At 55°S, the cumulative defrosted mass with $\varepsilon = 0.99$ (resp. $\varepsilon = 0.91$) is 159 kg m^{-2} (resp. 177 kg m^{-2}). This difference represents 13% of the total mass and should accelerate the crocus date by a shift of -2.4°Ls. These values are small compared to the difference in crocus dates of ≈20° between the cryptic and anti-cryptic sectors.

In conclusion, the effect of emissivity is negligible in the asymmetry of the SSPC recession.

4.1.7 Albedo in the visible range

As an approximation, we estimate the bolometric albedo A_{vis} in the visible range following the procedure exposed in section 2.4. In that case, we implicitly assume that the variability of the albedo with the observation conditions (observation geometry, lighting condition) is weak compared to the variability linked with the surface physical properties.

In order to be compatible with our model, we average the observed OMEGA albedo for each bin, according to our reference grid (section 3.4) with a integration time step of Ls=5°. This albedo is noted A^B_{vis}.

@@@@ FIGURE 7

Different investigations conducted in the visible and in the near IR have shown that the SSPC is asymmetric in albedo (James et al., 1979; Kieffer et al., 2000). Figure 7 shows that OMEGA measurements confirm this conclusion. The A^O_{vis} of the cryptic sector is 20 to 60% lower than the albedo of the anti-cryptic sector. This leads to a sublimation rate that can be up to three times higher.

We observe that the crocus date at latitude 85°S occurs 29°Ls later at 270°-280°E longitude than at 140°-150°E. This seems to be very well correlated with the difference in observed albedo (Fig. 7). In addition, the divergence, between the cryptic and anti-cryptic sectors, of the albedo evolution and the crocus line recession occur nearly simultaneously at Ls≈220° (see section 4.1). Therefore, albedo seems to be a good candidate to explain the asymmetry in the SSPC recession. This qualitative result will be tested quantitatively in the next section. The origin of the albedo asymmetry, such as frost deposition, dust content, cleaning process and slab ice, will be discussed in section 5.

4.1.8 Quantitative test

We tested the global coherence between the D-frost model (described in sections 3.2 and 3.3), the mean latitudinal propagation of the crocus line with time $T^O_{end}(L', \phi)$ (see Fig. 4), the bolometric albedo A^B_{vis} estimated by OMEGA (see section 2.4) and the GRS and HEND net CO_2 latitudinal accumulation curves $M^H_{CO_2/tot}(\phi)$ at the end of winter (Litvak et al., 2007; Kelly et al., 2006). As before, we consider two reference sectors of longitude (cryptic and anti-cryptic).
The albedo $A_{vis} = A_{vis}(L, \phi, Ls)$ is a field depending on longitude, latitude and time (expressed here in °Ls) that is only sparsely sampled in space and time by our observations. As a consequence, we parametrize A_{vis} using simple laws for its dependencies with latitude and time, according to two basic scenarii.

- Time independent albedo (model M2), where $A_{vis}(L, \phi, Ls) = A_{vis}^{M2}(L', \phi)$. L' represents the considered longitude sector domain, cryptic or anti-cryptic, ϕ is the latitude. This scenario assumes that the seasonal polar cap has latitudinal variations of albedo that do not change with time (Ls). We reproduce different regression speeds of the crocus line by modulating the latitudinal distribution of energy absorbed by the frost since the beginning of the sublimation phase. For instance, an acceleration of the crocus line corresponds to the crossing of a region with a lower albedo than the adjacent regions at lower latitude.
- Latitude independent albedo (model M3), where $A_{vis}(L, \phi, Ls) = A_{vis}^{M3}(L', L_s)$. The same definition is used for L'. This scenario assumes that the seasonal polar cap has a constant latitudinal albedo that does change with time (Ls). We reproduce different regression speeds of the crocus line according to time and longitude by modulating the temporal repartition of the energy absorbed by the frost since the beginning of the sublimation phase. For instance, an acceleration of the crocus line corresponds to a simultaneous decrease of the albedo for the whole remaining cap.

In both cases we consider flat and horizontal surfaces, but use realistic altitudes.

4.1.8.1 Time independent Albedo (model M2) For a given latitude ϕ, we compute the *equivalent albedo* $A_{vis}^{M2}(L', \phi)$ required to sublimate the CO_2 frost initial mass $M_{CO_2/tot}^{H}(\phi)$ measured by HEND/GRS, in the interval of time $[T_{beg}^{M2}(L', \phi), T_{end}^{O}(L', \phi)]$. The date $T_{beg}^{M2}(L', \phi)$ is the beginning of the net sublimation, when the local mass balance becomes negative in our model (Eq. 12), whereas $T_{end}^{O}(L', \phi)$ is the crocus date determined by OMEGA (end of the sublimation phase, Fig. 4). The error bar on the equivalent albedo is mainly defined by the error bar on the initial mass. We use a high emissivity, $\varepsilon = 0.99$, and a low albedo in the thermal IR, $A_{IR} = 0.01$, in order to estimate the lower limit of the equivalent albedo. We show in section 4.1.6 that the effect of emissivity in its realistic range of occurrence (between 0.91 and 1) is minor on the defrost mass and thus on the equivalent albedo.
We test the validity of the model by evaluating (i) the agreement between the equivalent albedo $A_{vis}^{M2}(L', \phi)$, estimated for the four latitudes at 85°S, 75°S, 65°S and 55°S in concordance with the HEND study (Litvak et al., 2007), and the observed albedo $A_{vis}^{B2}(L', \phi) = \left\langle A_{vis}^{B}(L', \phi, Ls) \right\rangle)$, averaged over the whole recession period, (ii) the agreement between $T_{beg}^{H}(\phi)$, the date of the beginning of the net sublimation according to HEND, and this same date $T_{beg}^{M2}(L', \phi)$, according to the model.

The first evaluation (i) can be done be analyzing Fig. 8, showing albedo vs. latitude for the cryptic and anti-cryptic sectors.
For both sectors, there is a general agreement between $A_{vis}^{M2}(L', \phi)$ and the

time averaged albedo $A^{B2}_{vis}(L', \phi)$ observed by OMEGA. Albedo increases with latitude, more strongly for the anti-cryptic sector than it does for the cryptic sector. The high dispersion of the albedo around 85°S in the cryptic sector is due to the high variability of ice type (slab ice, frost and mixing with dust) with time in this region (Kieffer et al., 2000; Piqueux et al., 2003; Langevin et al., 2006; Kieffer et al., 2006).

@@@@@ FIGURE 8

The second evaluation (ii) is done through the analysis of Tab. 4 and 5. We can analyze the match between $T^{H}_{beg}(\phi)$ and $T^{M2}_{beg}(L', \phi)$ as an indicator of the validity of our scenario. The agreement is relatively good at low latitude ϕ for both sectors L'. The misfit increases as latitude increases. The effect of slope may be at the origin of this effect. For latitudes higher than 65°S, solar illumination becomes more grazing and the effect of slope may no longer be negligible. This effect does not affect the global defrosted mass, but changes the date of the beginning of sublimation for equator facing facets.

In conclusion, the model shows good consistency between the different different datasets, i.e. albedos observed by OMEGA, crocus lines observed by OMEGA, net accumulation measured by HEND/GRS and altitudes measured by MOLA. Nevertheless, the low spatial resolution in latitude of the HEND/GRS measurements precludes the full testing of this model.

4.1.8.2 Latitude independent albedo (model M3) This second scenario (model M3) is based on a simple model of albedo $A^{M3}_{vis}(L', L_s)$, depending on longitude (cryptic/anti-cryptic) and time. It does not have the limitation of latitude resolution implied by the use of HEND/GRS data. Based on the OMEGA images, we determine two empirical laws of temporal evolution for the albedo of the cryptic and anti-cryptic sectors (Fig. 9). For the cryptic sector (longitudes between 60° and 260°E) is (mean=0.0000; variance =0.0012):

$$A^{M3}_{vis}(Ls) = -0.1967 + 0.0029 \times Ls \tag{18}$$

For the anti-cryptic sector (longitude between 100°W and 60°E) (mean=-0.0067; variance = 0.0013):

$$A^{M3}_{vis}(Ls) = \min\left(-0.3920 + 0.0044 \times Ls, 0.63\right) \tag{19}$$

The albedo increases with time until Ls=230°. The increase is much larger for the anti-cryptic sector than for the cryptic sector. Both laws fit well with the observed albedo $A^{B3}_{vis}(L', Ls) = \left\langle A^{B}_{vis}(L', \phi, Ls)\right\rangle)$ averaged in latitude, as a function of time (Fig. 9).

We test the validity of this scenario by evaluating (i) the agreement between the sublimated CO_2 mass $M^{M3}_{CO_2/tot}(L', \phi)$ predicted by the model M3 and the mass $M^{H}_{CO_2/tot}(\phi)$ measured by GRS/HEND; (ii) the agreement between the date $T^{M3}_{beg}(L', \phi)$, the date of the beginning of the net sublimation according the model M3, and $T^{H}_{beg}(\phi)$, the same according to HEND.

@@@@ FIGURE 9

We invite the reader to perform the first evaluation (i) by studying Tab. 4 and 5. The mass $M^{M3}_{CO_2/tot}(L', \phi)$ predicted by the model fits well within the error-bar of the measured masses $M^{H}_{CO_2/tot}(\phi)$.

The second evaluation (ii) can be done using the same Tab. 4 and 5. The agreement between $T^{H}_{beg}(L', \phi)$ and $T^{M3}_{beg}(L', \phi)$ is good at low latitudes for both sectors. However, the misfit increases as latitude increases. Again, the explanation is that the slope effect increases with latitude. At this point, the latitude independent scenario M3 is preferable compared to the time independent scenario M2 because it does not suffer from the coarse latitude resolution imposed by GRS.

@@@ TABLE 4

@@@@ TABLE 5

In conclusion, confronting the model with the observations shows that the albedo is the most determinant parameter and that it increases globally during the recession for both (albeit differently) the cryptic and anti-cryptic sectors. The relative agreement between the model and the observations (Langevin et al. (2006)), in particular for the cryptic sector, suggests that all the solar energy absorbed by the mineral substrate underlying the CO_2 ice slab and/or the upper layer of dust contamination should be transferred efficiently to the CO_2 deposits for their sublimation. Future investigations should take into account the time and space variations of the albedo field, but this is not possible with OMEGA because the sampling is very sparse. Other datasets, such as MOLA or MOC, should help to achieve accurate modeling of the SSPC recession.

4.2 SSPC recession at local scale

Already at the end of the XIXth century, the irregular SSPC waning was noticed via telescopic observations by Campbell, 1895. Using Mariner 9 photographs, Veverka and Goguen, 1973 concluded that surface topography controls this irregularity. Here we characterize the edge structure of the SSPC by

the snowdrop distance that we evaluate thanks to meridian profiles of CO_2 detection by OMEGA.

In section 2.3, we define the inner and outer crocus lines for a given date (Ls) as well as the inner and outer crocus dates for a given latitude. The time elapsed between these two dates is the snowdrop time. According to OMEGA CO_2 ice detection, the snowdrop time ranges from a few °Ls to more than 40°Ls depending on location and time. In this section, we will discuss the origin of this phenomenon.

We will address the following key questions. Is the local variability of snowdrop time due to local variations of accumulation ? subsurface annual heat wave ? CO_2 ice stability linked with altitude differences ? radiation absorption controlled by roughness ? difference in albedo in the visible range ? difference in emissivity/albedo IR ? These variations typically occur at spatial scales on the order of 1 km. For that purpose, we seek correlations between the variations of the snowdrop time and the previous parameters.

4.2.1 Statistical index

The inner and outer crocus lines are defined on the basis of spatial bins (see Fig. 1). The appearance of the first 1% of defrosted pixels defines the inner crocus date whereas the disappearance of the last 1% of frosted pixels defines the outer crocus date. Thus, the snowdrop time is a measure of the time elapsed between these two extreme defrost situations. In other words, the snowdrop time is an estimation of the distribution width of T_{end} inside the bin. Such a distribution is a function of three distributions, namely the initial CO_2 mass $M_{CO_2/tot}$, the date of the beginning of the sublimation T_{beg} and the mass flux of sublimation $\frac{\partial M_{CO_2}}{\partial t}$. If these distributions inside the bin are narrow, all facets will defrost at almost the same time and the snowdrop time will be short. On the contrary, if these distributions inside the bin are wide, all facets will defrost at different times and the snowdrop time will be long. In short, the snowdrop time must be correlated with a combination of the three distributions $M_{CO_2/tot}$, T_{beg} and $\frac{\partial M_{CO_2}}{\partial t}$.

We propose to describe the distribution width of the random variable X, with N occurrences named X_i, with the following statistical parameter:

$$\hat{P_{stat}}(\mathrm{X}) = \frac{\sqrt{\hat{\sigma}}}{\hat{\mu}} \tag{20}$$

$\hat{\mu}$ and $\hat{\sigma}$ being the usual estimators of the mean and variance:

$$\hat{\mu} = \frac{1}{N}\sum_{i=1}^{N} \mathrm{X_i} \tag{21}$$

$$\hat{\sigma} = \frac{1}{N-1}\sum_{i=1}^{N} (\mathrm{X_i} - \hat{\mu})^2 \tag{22}$$

Now we define a statistical index $R_{stat}(\mathrm{X})$ that describes the discrepancy between the lower and upper parts of the population of the distribution of X. Assuming that X is Gaussian, 32% of the population should be outside the range $[\hat{\mu}-\sqrt{\hat{\sigma}},\hat{\mu}+\sqrt{\hat{\sigma}}]$, with 16% in the bottom wing and 16% in the top wing. The lower limit of the ratio between an occurrence of the upper population and an occurrence of the lower population is:

$$R_{stat} = \frac{\hat{\mu}+\sqrt{\hat{\sigma}}}{\hat{\mu}-\sqrt{\hat{\sigma}}} = \frac{1+\hat{P_{stat}}}{1-\hat{P_{stat}}} \tag{23}$$

Assume that $M_{CO_2/tot}$ and T_{beg} take a unique value. If we estimate that $\hat{P_{stat}}$ for the defrost mass flux $\frac{\partial M_{CO_2}}{\partial t}$ inside a bin is equal to 0.4, it means that 16% of the population (upper wing) will have a sublimation time duration T_{end} half of the other 16% (lower wing).

Now we must test the correlation, for a given latitude and longitude range, between the snowdrop time (distribution width of T_{end}) and the the statistical index $\hat{P_{stat}}$ of (i) the initial accumulated mass $M_{CO_2/tot}$; (ii) the date of the beginning of the sublimation T_{beg}; (iii) the mass flux $\frac{\partial M_{CO_2}}{\partial t}$ or any physical parameter that controls it. In the special case of the albedo (that partly controls $\frac{\partial M_{CO_2}}{\partial t}$), we sort all pixels of the OMEGA observations from Ls=0° to 360° in the bins of our geographical grid (see section 3.4) and by intervals of 5° Ls. Then we calculate for each bin containing pixels the mean $\hat{\mu}$, the variance $\hat{\sigma}$ and the statistical index $\hat{P_{stat}}$ of the albedo.

4.2.2 CO_2 ice accumulation $M_{CO_2/tot}$

The total CO_2 ice accumulation, previously discussed at global scale in section 4.1.1, can vary at local scale.
According to Eq. 16, the local scale variation of accumulation depends on different terms which can have a local expression, namely (i) thermal emission controlled by temperature and emissivity; (ii) atmospheric heat advection; (iii) subsurface heat conduction which depends on slope, albedo and thermal inertia of the subsurface; (iv) absorbed radiation linked with the VIS and IR

albedos, slope, and roughness.
The accurate modeling of accumulation at local scale, including atmospheric dynamic effects, lies outside the scope of this paper. Thermal inertia observed by TES is uniform near the South Pole (Putzig et al., 2005). In this study, we will assume that accumulation varies smoothly with latitude, as measured by HEND (Litvak et al., 2007). This apparent smoothness could be an effect of the large instrument footprint. Thus ambiguities between $M_{CO_2/tot}$, on the one hand, and T_{beg}, $\frac{\partial M_{CO_2}}{\partial t}$, on the other, will not be resolved properly in this work.

4.2.3 Date of the beginning of sublimation T_{beg}

As discussed in section 4.1.2, T_{beg} is related to all terms of Eq. 16. In the next models, T_{beg}will be a free parameter, set by the model itself.

4.2.4 Annual heat wave in the ground

As previously discussed in section 4.1.3, the maximum sublimated mass due to the annual heat wave in the ground represents 6% of the total sublimated mass (at latitude 55°S) leading to a shift of the crocus date of less than 2°Ls. For comparison, the maximum snowdrop time is more than 40°Ls. This energy source can thus be neglected at a first order in all discussions concerning the recession phase even at local scale.

4.2.5 Altitude

The effect of altitude, as previously discussed in the section 4.1.4, is very low at global scale. At local scale, the typical standard deviation of altitude inside a bin is between 10 m and 1000 m. We estimated the effect of a 1000 m difference in altitude for two extreme points of the anti-cryptic sector. At 85°S, an increase in altitude of 1000 m from the 2500 m level leads to a increase of defrosted mass of 13 kg m^{-2} during the complete recession time. The corresponding snowdrop time delay is 0.5°Ls. At 55°S, from the 1000 m level, the defrosted mass increase represents 7 kg m^{-2} and a snowdrop time delay of 1°Ls, much less than most observed snowdrop times. The altitude effect alone is not sufficient to explain the snowdrop time evolution in space and time.

4.2.6 Radiation budget on a rough surface

In order to estimate the effect of surface roughness on the local daily absorbed radiation W (Eq. 4), we compute it using the model presented in section 3.2.

We set the albedos $A_{vis} = 0$, $A_{IR} = 0.01$ and the emissivity $\varepsilon = 0.99$, a configuration that maximizes the effect of slope and shadow on all radiation terms. Slope and altitude given by the MOLA database are at a resolution of 920 m. If roughness of the Martian surface is the parameter that controls the recession at local scale, the snowdrop time and the local statistical index $\hat{P_{stat}}$ for the daily absorbed radiation must correlate. Figure 10 represents the statistical index $\hat{P_{stat}}$ along two meridian profiles (a) 260°-270°E and (b) 270°-280°E.

@@@ FIGURE 10

In both Fig. 10 (a) and (b), we can note that the effect of slope distribution on the variability of absorbed radiation is particularly noticeable when the sun elevation at local noon is low. On profile (a), the maximum snowdrop time (about 30°Ls) occurs at latitude 85°S, but does not correlate with high values of the statistical index $\hat{P_{stat}}$. On profile (b), the snowdrop time is constant (about 10°Ls) despite the fact that the statistical index at the crocus line decreases with time. It seems that the snowdrop time is independent of the local absorbed radiation modulated by surface roughness. This result stands for all other directions around the geographic South Pole.

In order to completely reject the hypothesis of the surface roughness effect, the snowdrop time must be compared with the local distribution of defrost mass rather than with the radiation budget. Section 4.2.9 will discuss this point.

4.2.7 Emissivity and albedo in the thermal infra-red

As discussed in section 4.1.6, emissivity likely ranges from 0.91 to 1.0 for CO_2 ice. Using the same calculation at both 85°S and 55°S, we can estimate the effect of emissivity distribution on snowdrop time. If emissivity is distributed between these two extreme values, the snowdrop time is increased by 1.6°Ls at 85°S and 2.4°Ls at 55°S. This is not enough to explain the local variations of snowdrop time. Emissivity cannot be the key parameter that controls the SSPC recession at local scale.

4.2.8 Albedo in the visible range

In order to estimate the effect of albedo on the snowdrop time, we estimate its distribution from our selection of OMEGA observations arranged into bins. We use the absorption factor $Abs_{vis} = 1 - A_{vis}$ that appears in Eq. 6. As an approximation, we estimate the bolometric albedo A_{vis} with $A^O_{vis} = 1 - Abs^O_{vis}$ (see Eq. 2). If the albedo is the parameter that controls the recession at local scale, snowdrop time and the local statistical index $\hat{P_{stat}}$ of Abs^O_{vis} must be correlated.

We choose to represent in Fig. 11 six typical meridian profiles to illustrate the test of our hypothesis, namely (a) 0°-10°E, (b) 70°-80°E, (c) 200°-210°E, (d) 260°-270°E, (e) 270°-280°E and (f) 320°-330°E. We restrict the time window of this investigation to Ls=220°-330° because, before Ls=220°, pollution by atmospheric dust and water ice is likely (see section 2.4) and their contribution to $R^{O}_{1.07}$ will affect its correspondence with surface albedo.

@@@@@ FIGURE 11

On profile (a), the snowdrop time is maximum (about 40°Ls) at 84°S and correlates with a high value of $\hat{P_{stat}}$ present at this latitude since Ls=255°.

On profile (b), the snowdrop time is intermediate (about 15°Ls) from 75°S to 83°S, where $\hat{P_{stat}}$ is low. At latitudes between 83°S and the pole, the snowdrop time reaches 30°Ls and is well correlated with a local high $\hat{P_{stat}}$.

Profile (c) presents a uniform snowdrop time of about 10-15°Ls and the estimation of $\hat{P_{stat}}$ is low.

On profile (d), from latitude 84°S to 86°S and starting at Ls =220°, albedo is very dispersed with high $\hat{P_{stat}}$ values. This is correlated with a very high snowdrop time of more than 30°Ls.

Profile (e) shows the most homogeneous snowdrop time (10°Ls) of all profiles around the south pole, in agreement with constantly low levels of $\hat{P_{stat}}$.

On profile (f), we note three very distinct regimes of albedo dispersion. At latitudes below 78°S, $\hat{P_{stat}}$ is close to zero. Between 78°S and 80°S, $\hat{P_{stat}}$ is higher than 20% starting at Ls=220°. Between 82°S and 87°S, $\hat{P_{stat}}$ increases with time. This is correlated with a low snowdrop time for the first part (less than 10°Ls) and a high snowdrop time (more than 20°Ls) for the second as well as the third regimes.

Another phenomenon occurs on all profiles, as suggested by close examination of $\hat{P_{stat}}$. The albedo dispersion increases just before the transition zone. This is easily explained by the fact that subpixel mixing occurs at this time and that OMEGA sees pixels with various levels of sub-pixel mixing and thus various albedo, all with positive detection of CO_2. This is particularly obvious on profiles (a), (d), (e) and (f) where the global albedo level is high and the subpixel mixing can produce a high variance.

@@@@@ FIGURE 12

Local dispersions of albedo show a quasi-systematic correlation with the snowdrop time. This result is also valid for all other directions around the geographic South Pole. For the complete dataset, the correlation coefficient be-

tween the snowdrop time and the statistical parameter $\hat{P_{stat}}$ calculated for the 22.5-18.5°Ls albedo before the inner crocus date at a given location is 0.640 (see Fig. 12). We conclude that albedo is likely the key parameter that controls the SSPC recession at local scale.

4.2.9 Quantitative test

In sections 4.2.4 to 4.2.8 we have shown that:

- local variations of subsurface heat flow, altitude and emissivity alone cannot control the snowdrop time for a given latitude since their influence on the cumulative mass of sublimated CO_2 is weak compared to the influence of other factors,
- the snowdrop time is well correlated with the local variability of albedo whereas it is not with the absorbed radiation variability due to the slope distribution alone.

In order to confirm the prevailing nature of the albedo, we perform a more detailed simulation of the cumulative mass of sublimated CO_2 frost for each facet of our geographical grid. We take the altitudes and slopes from the MOLA data at a resolution of 920 m. Conversely, we ignore the local variation of the albedo by taking a homogeneous value that increases with time, i.e. the latitude independent scenario, model M3 (see section 4.1.8) for the whole cap. At global scale, such a simplified model allowed us to reproduce the recession of the mean crocus line (section 4.1.8). All the other parameters are set to the standard values given in section D.
If surface roughness is the parameter that controls the recession at local scale, the snowdrop time and the local statistical index $\hat{P_{stat}}$ of the daily defrost mass $\frac{\partial M_{CO_2}}{\partial t}$ must be correlated.

In Fig. 13, we choose to represent the spatio-temporal behavior of $\hat{P_{stat}}$ for the six meridian profiles and the time window already considered in section 4.2.8, namely (a) 0°-10°E, (b) 70°-80°E, (c) 200°-210°E, (d) 260°-270°E, (e) 270°-280°E and (f) 320°-330°E.

@@@ FIGURE 13

On profile (a), the snowdrop time is maximum (about 40°Ls) at 84°S and is well correlated with a high value of $\hat{P_{stat}}$ already present starting at Ls=220°. There is also a correlation with a high dispersion of albedo (section 4.2.8), but at 79°S, a high snowdrop time occurs with a low $\hat{P_{stat}}$.

On profile (b), the snowdrop time is intermediate (about 15°Ls) from 75°S to 83°S, when $\hat{P_{stat}}$ is latitude dependent. At latitudes above 83°S, the snowdrop time reaches 30°Ls and is anti-correlated with $\hat{P_{stat}}$.

From 80°S to 90°S, profile (c) presents a homogeneous intermediate snowdrop time of about 10-15°Ls corresponding to very low values of $\hat{P_{stat}}$.

On profile (d) from latitude 84°S to 86°S and starting at Ls =220°, the defrosted mass is very uniform from place to place (low values of $\hat{P_{stat}}$). This is anti-correlated with a very high snowdrop time of more than 30°Ls.

Profile (e) shows the best constant snowdrop time (10°Ls) of all profiles around the South Pole despite the fact that the dispersion of defrosted mass $\hat{P_{stat}}$ strongly fluctuates with latitude.

On profile (f), no correlation between defrosted mass $\hat{P_{stat}}$ and snowdrop time appears. For instance, at latitudes between 78°S and 80°S, the snowdrop time is more than 20°Ls and $\hat{P_{stat}}$ is close to zero. Very close to latitude 84°S, the statistical index $\hat{P_{stat}}$ is always higher than 2%, but no increase of the snowdrop time is observed.

@@@@@ FIGURE 14

For the complete dataset, the correlation coefficient between the snowdrop time and the statistical parameter $\hat{P_{stat}}$ calculated for the daily defrost mass at 22.5-18.5°Ls before the inner crocus date at a given location is 0.358 (see Fig. 14).

This quantitative test confirms that the combined effects of altitude distribution, slope distribution and surface roughness on the defrost mass distribution are not sufficient to explain the variability of the snowdrop distance. Albedo remains the most pertinent parameter. This result stands for all other directions around the geographic South Pole.

5 Discussion

At global scale, the asymmetry of the SSPC recession around the geographic South Pole is due only to the albedo asymmetry. Indeed it can be reproduced by our defrost mass model with only two asymmetrical parameters, the mean crocus date and albedo with the latter increasing with time. In the model, the initial mass at the end of winter is symmetrical, in agreement with the measurements made via the loss of neutron flux (Litvak et al., 2007) or gamma rays (Kelly et al., 2006). Nevertheless, asymmetry in the accumulation process remains an alternative possibility that our study cannot rule out completely. The time dependence of the equivalent albedo is in very good agreement with the OMEGA observations. This fact makes us confident that our model is valid at a first order. We have shown that neither the effect of the annual heat

wave, nor the altitude, the surface roughness or the emissivity are important compared to the albedo effect. Thus albedo is the key parameter that controls the recession SSPC at global scale.

At local scale, we describe the fine structure of the SSPC edge with inner and outer crocus lines, the two being separated by the snowdrop distance. Since the SSPC recession involves space and time, all those indicators have an equivalent in the temporal domain, i.e. inner and outer crocus dates, snowdrop time. We concluded in section 4.2 that the local albedo distribution which characterizes a region at a given latitude is the key parameter that controls the SSPC disappearance several weeks later.

The effect of surface roughness at a scale lower than the resolution of the MOLA data could be relevant, but is not tested in this work. The test may be done in the future trying to address the difficulties of extrapolating to the 1 m scale (Campbell et al., 2003).

At both global and local scales, albedo is the most pertinent parameter that controls the seasonal South Polar cap recession. Different physical parameters can induce asymmetry or variability in the albedo field.

- Subpixel mixing. Inside the footprint of the OMEGA instrument, a linear mixture as well as an intimate mixture of bright frost and dark rock/dust materials could occur. Such mixtures can produce an apparent albedo variability if quantities inside the pixel are variable.
- Grain size. As suggested by Warren et al., 1990, grain size significantly reduces albedo especially if the ice is slightly contaminated by a strong absorber. More recent calculations (Hansen, 1999; Douté et al., 2008a,b) using an optical constant of higher accuracy (Hansen, 1997; Schmitt et al., 1998) mitigate, but do not rule out this effect for pure ice. An extreme situation occurs when the SSPC deposits are made of a slab of pure CO_2 ice, so transparent that a large fraction of photons can reach the bottom and be absorbed by the dust substratum, thus producing a low visible albedo. This extreme scenario was suggested for the cryptic region from TES data (Kieffer et al., 2000). At this point, we should note that OMEGA observations also suggest the presence of slab ice outside the cryptic region (Langevin et al., 2006). For instance, at latitude 59°S in the anti-cryptic region (longitude 344°E) the albedo of the icy terrains is only 20%.
- Dust content. As suggested by Warren et al., 1990, dust within ice deposits significantly reduces albedo.
- Ice thickness. As suggested by Warren et al., 1990, the albedo of an optically thin CO_2 granular layer has a positive correlation with the snow depth.

Different processes can produce a global asymmetry and/or local variability of the previous physical parameters.

5.1 Subpixel mixing

The temperature of a completely defrosted terrain can go up to 300 K, a temperature which strongly increases its thermal emission, in particular towards the surrounding still frozen terrain, thus accelerating their sublimation.

Subpixel mixing should happen between the inner and outer crocus dates as suggested in section 4.2.8. But subpixel mixing is not a good scenario for the whole SSPC because that would lead to a recession velocity much higher than observed. In the longitude sector 320°-330°E, the high albedo dispersion is present at least 40°Ls before the crossing of the inner crocus line (see Fig. 11).

5.2 Ice deposition process

During the phase of CO_2 frost accumulation, the SSPC is mainly formed by direct condensation, but some snow events can occur (Forget et al., 1998). GCM studies show that a topographic forcing by the Hellas basin creates an asymmetry in the mode of deposition. Precipitation events are more frequent for the anti-cryptic sector than for the cryptic sector (Colaprete et al., 2005; Giuranna et al., 2008). This suggests that the texture should be more granular (smaller grain sizes) for the former compared to the latter. This texture difference produces a relatively higher albedo in the anti-cryptic region.

Local topographic forcing could create local variability of snow precipitation (Colaprete and Toon, 2002), leading to a variability of grain size and ice thickness. No simulation has been done yet by GCM at local scale for the South Polar region, but this effect is a good candidate to explain the local variability of albedo.

During the SSPC recession, recondensation during the night can occur and the new condensate would cover dusty ices, enhancing the albedo. This process, that likely happens at local scale, tends to decrease albedo variability.

The usual defrost mass balance proposed in section 3.3.1 can produce local differences of defrost mass due to slope orientation, shadows or altitude. However, the statistical index of these parameters is not correlated with that of albedo. Thus, slope orientation, shadows or altitude effects are not likely to produce relevant thickness distribution.

5.3 Metamorphism

Metamorphism tends to increase the optical mean free path within the ice through both grain growth and ice sintering, leading to an apparent grain size larger than the physical grain size (Eluszkiewicz, 1993). Thus, metamorphism tends to decrease albedo. This model shows that metamorphism is controlled by ice temperature, but could also be enhanced by the vertical distribution of solar energy absorption, boosting the internal vapor transport (sublimation, recondensation). At this time, there is a lack of experimental results to constrain the CO_2 metamorphism regime on Mars.

Nevertheless, the differential boost by differential solar energy absorption, modulated by slopes and shadows, cannot explain either the asymmetry or the local variability of albedo. At global scale, both cryptic and anti-cryptic sectors undergo this effect with the same magnitude (Fig. 6). At local scale, there is no correlation between the snowdrop time and the radiation budget distribution (Fig. 10 and 11).

The differential boost may be relevant only if there is a difference in albedo, controlled for instance by grain size or dust load, leading to a difference in the amount of absorbed energy. There is a strong positive feedback between albedo and metamorphism. Lower albedo induces more solar energy absorbed, induces stronger metamorphism, induces higher grain size, induces lower albedo. Such a process can enhance small differences. For instance, metamorphism may be appropriate to enhance initial asymmetry due to grain size or initial local variability due to difference in dust load.

5.4 Dust precipitation

The dust content within the ice deposit can be incorporated during the accumulation phase or can be added later due to dust precipitation. Different scenarios could imply various dust sources such as the atmosphere or local geysers.

If dust particles have an aeolian origin, they can be deposited in variable amounts due to differential dust loading in the atmosphere. Furthermore, surface wind can reshuffle the dust on the ground, leading to local variability of albedo.

An alternative scenario, more likely to occur in the cryptic region (Piqueux et al., 2003; Kieffer et al., 2006), implies CO_2 geysers ejecting dust at the surface of the ice. Piqueux et al., 2003 suggest that this process is at the origin of the asymmetry in albedo at global scale. In addition, the detection of

optically thick, but thermally thin dark materials, that would overlay a layer of CO_2 ice and thus would be kept at low temperatures, has been recently suggested by Langevin et al., 2006 for the cryptic region.

Moreover, there is a positive feedback involving albedo and dust content. More dust induces lower albedo, induces more solar energy absorbed, induces faster sublimation, induces less thickness, induces lower albedo. Such a mechanism tends to increase differences in albedo.

5.5 Cleaning process

Some authors found a correlation between albedo of the residual ice cap and insolation (Paige and Ingersoll, 1985; Kieffer et al., 2000) and claim that a cleaning process, controlled by insolation, progressively frees the ice from its dust. Different candidate processes can occur on the residual ice cap, but on the seasonal cap too, depending on the dust particle size. Dust can burrow through the ice or be ejected in the atmosphere (Kieffer et al., 2000; Portyankina and Markiewicz, 2003). Such mechanisms increase the albedo by decreasing the dust content within the ice deposit.

However, these mechanisms alone cannot explain the asymmetry or the local variability of albedo. Both cryptic and anti-cryptic sectors should be cleaned with the same intensity if the initial dust load is identical (Fig. 6). At local scale, the snowdrop time and the radiation budget distribution, which would govern the magnitude of the cleaning process, are not correlated (Fig. 10 and 11).

However, differences of dust load/size/shape distribution at the top of the CO_2 ice layer associated with the cleaning process can be a clue to explain the variability of albedo. Nevertheless, there is a negative feedback between albedo and cleaning. Lower albedo induces more solar energy absorbed, induces stronger cleaning, induces higher albedo. Such a mechanism tends to smooth differences in albedo.

5.6 Mechanical ablation

A process of mechanical ablation of the ice deposits, caused by atmosphere turbulence, would decrease the ice thickness and the albedo. In this scenario, suggested on Earth for the formation of the blue ice area by catabatic winds in Antarctica (Bintanja, 1999), turbulence is linked with wind and surface roughness. Due to the low density of the atmosphere on Mars, this effect is

likely only for small ice particles. Thomas et al., 1979 is of the opinion that some frost streaks have a wind origin.

6 Conclusions

We introduce and use a CO_2 ice sublimation model called D-frost and estimate its validity at global scale using (i) the accumulation estimated by GRS/HEND, (ii) the date of the end of sublimation estimated by OMEGA, (iii) the CO_2 ice albedo estimated by OMEGA. We propose two ways to test model consistency, namely time independent albedo (model M2) and latitude independent albedo (model M3). In both cases, albedo increases with time and the model matches the observations.

We also introduce the snowdrop time/distance to characterize the SSPC edge. This new quantity, complementary with the crocus date/line, is a new and promising observable to constrain efficiently the Martian GCM.

We propose an efficient way to calculate the CO_2 ice sublimation mass using D-frost in a case of rough surfaces, taking into account statistically the shadow induced by the topography. We show that the snowdrop time is correlated with the albedo distribution. Also we estimate a very low level of correlation between (i) the snowdrop time and (ii) the sublimated mass distribution due to surface roughness estimated by the model. This suggests that the effect of topography can be neglected at a first order.

In conclusion, we show that the CO_2 ice sublimation in the SSPC is mainly controlled by albedo at both global and local scales, but additional investigations are required to point out the major processes controlling this quantity. One suggestion would be the use of other datasets, such as MOLA or MOC, to study in more detail the dependence of the increasing albedo trend with latitude, longitude and time. In addition, a modeling effort of ice cloud precipitation at local scale and geyser activity is necessary. Also, several experiments should be designed to measure the modalities and magnitude of CO_2metamorphism, cleaning process and mechanical ablation. Finally, the physical analysis of the OMEGA and CRISM observations with surface radiative transfer models should produce quantitative maps of surface properties of the SSPC that will greatly help to understand the physical process acting to produce the observed albedo, crocus line and snowdrop distance.

A Scales of interest

bin: element of the geographical grid drawn regularly in longitude and latitude on the planetary surface. Sampling is 10° in longitude (from 0°E to 360°E) and 0.3° in latitude (from 53°S to 90°S).

meridian profile: sequence of values taken by a parameter along a meridian (constant longitude) for consecutive bins which span 10° in longitude. Latitudinal range covered is 53°S to 90°S for the model and from 30°S to 90°S for the OMEGA observations.

The bins are at a lower resolution than following objects:

facet: pixel in MOLA data that is used for the calculation of the insolation modulated by roughness. Spatial resolution is 920 m in a South Polar stereographic projection,

pixel: element of detection in the OMEGA observations, the spatial resolution can vary from 2 km to 700 m.

B Integration of insolation

Unfortunately, the direct and indirect solar illumination Q_{sun} and Q_{scat} can be negative depending on L. Thus we multiply these two terms with a door function Π that bounds the integration of the absorbed energy to the interval of L values $[L_{min}, L_{max}]$when it is positive (when the facet is illuminated).

$$\Pi_{L_{min}}^{L_{max}}(L) = \begin{cases} 1,\ for\ L_{min} < L < L_{max} \text{where} \overrightarrow{n_{surf}}.\overrightarrow{r_{sun}} \geq 0 \\ 0,\ otherwise \end{cases} \tag{1}$$

$$\overrightarrow{r_{surf}} \bullet \overrightarrow{r_{sun}} = \sin(\phi)\sin(\delta) + \cos(\phi)\cos(\delta)\cos(L-\alpha) \tag{2}$$

$$\overrightarrow{n_{surf}} \bullet \overrightarrow{r_{sun}} = \sin(\phi_n)\sin(\delta) + \cos(\phi_n)\cos(\delta)\cos(L_n-\alpha) \tag{3}$$

The N/S slopes along a meridian are given by the following relations:

$$\phi_n = \begin{cases} \pi - \phi - \phi',\ for\ \phi + \phi' > \frac{\pi}{2} \\ -\pi - \phi - \phi',\ for\ \phi + \phi' < -\frac{\pi}{2} \\ \phi + \phi',\ otherwise \end{cases} \tag{4}$$

and the W/E slopes along a parallel by:

$$L_n = L + L' + L_c \begin{cases} L_c = 2\pi,\ for\ L + L' < 0 \\ L_c = -2\pi,\ for\ L + L' > 2\pi \\ L_c = 0,\ otherwise \end{cases} \tag{5}$$

Using those relations:

$$\phi' = \arctan(-\frac{\partial topo}{\partial \phi}) \tag{6}$$

$$L' = \arctan(-\frac{\partial topo}{\partial L}) \tag{7}$$

We assume that insolation is null when the sun is on the opposite side of the facet. This condition corresponds to a virtual displacement of the considered surface point from its real longitude L to L_n.
Our assumption can be written:

$$\overrightarrow{n_{surf}} \bullet \overrightarrow{r_{sun}} \geq 0 \Leftrightarrow \cos(L_n - \alpha) \geq -\tan(\phi_n) tan(\delta) \tag{8}$$

There are 3 different solutions for the equations depending on latitude and slopes.

(1) The sun never rises:

$$\overrightarrow{n}_{surf} \bullet \overrightarrow{r_{sun}} < 0 \Leftrightarrow 1 < -\tan(\phi_n)\tan(\delta) \tag{9}$$

$$W = \frac{1}{2\pi}\int_0^{2\pi} Q_{sun}\Pi_0^0 + Q_{scat}\Pi_0^0 + Q_{IR}\Pi_0^0 + Q_{floor}\Pi_0^{2\pi} dL \tag{10}$$

(2) The sun never sets:

$$\overrightarrow{n}_{surf} \bullet \overrightarrow{r_{sun}} > 0 \Leftrightarrow -1 > -\tan(\phi_n)\tan(\delta) \tag{11}$$

$$W = \frac{1}{2\pi}\int_0^{2\pi} Q_{sun}\Pi_0^{2\pi} + Q_{scat}\Pi_0^{2\pi} + Q_{IR}\Pi_0^{2\pi} + Q_{floor}\Pi_0^{2\pi} dL \tag{12}$$

(3) There is a sunrise and a sunset on the facet:

$$\overrightarrow{n_{surf}} \bullet \overrightarrow{r_{sun}} > 0 \Leftrightarrow -1 \leq -\tan(\phi_n)\tan(\delta) \leq +1 \tag{13}$$

We can define H_{n0} the local horary angle on the facet:

$$\cos(H_{n0}) = -\tan(\phi_n)\tan(\delta) \tag{14}$$

In this case, the sun illuminates the facet only when:

$$\overrightarrow{n_{surf}} \bullet \overrightarrow{r_{sun}} > 0 \Leftrightarrow \alpha - H_{n0} < L_n < \alpha + H_{n0} \tag{15}$$

Using Eq. 5, the condition for L is:

$$L_{min} = \alpha - H_{n0} - L' - L_c < L < \alpha + H_{n0} - L' - L_c = L_{max} \tag{16}$$

$$W = \frac{1}{2\pi} \int_0^{2\pi} Q_{sun} \Pi_{L_{min}}^{L_{max}} + Q_{scat} \Pi_{L_{min}}^{L_{max}} + Q_{IR} \Pi_0^{2\pi} + Q_{floor} \Pi_0^{2\pi} dL \tag{17}$$

Analytical integration The following integrals can be solved analytically:

$$W_{scat} = \frac{1}{2\pi} \int_0^{2\pi} Q_{scat} \Pi_0^{2\pi} dL = Q_{scat} \tag{18}$$

$$W'_{scat} = \frac{1}{2\pi} \int_0^{2\pi} Q_{scat} \Pi_{L_{min}}^{L_{max}} dL = \frac{H_{n0}}{\pi} Q_{scat} \tag{19}$$

$$W_{IR} = \frac{1}{2\pi} \int_0^{2\pi} Q_{IR} \Pi_0^{2\pi} dL = Q_{IR} \tag{20}$$

$$W_{floor} = \frac{1}{2\pi} \int_0^{2\pi} Q_{floor} \Pi_0^{2\pi} dL = Q_{floor} \tag{21}$$

Property Using Eq. 2, 3, 5 and 7, we can see that Q_{sun} depends on L only through the scalar products:

$$Q_{sun} = F_1.F_2.F_3 \left(\cos(L - \alpha)\right).F_4 \left(\cos(L - \alpha + L' + L_c)\right).F_5 \left(\cos(L - \alpha)\right) \tag{22}$$

$$W_{sun} = \frac{1}{2\pi} \int_{\alpha+C}^{\alpha+D} Q_{sun}(L) dL = \frac{1}{2\pi} \int_C^D \tilde{Q}_{sun}(\tilde{L}) d\tilde{L} \tag{23}$$

with $\tilde{L} = L - \alpha$, $C = -H_{n0} - L' - L_c$, $D = H_{n0} - L' - L_c$ and $\tilde{Q}_{sun} = F_1.F_2.F_3 \left(\cos(\tilde{L})\right).F_4 \left(\cos(\tilde{L} + L' + L_c)\right).F_5 \left(\cos(\tilde{L})\right)$.
This shows that W_{sun} is independent of α, the longitude of the sub-solar point. We set this parameter to zero to estimate the integral 23.

C Summary of the parameter values used for the surface radiation budget

Model parameters. Units are noted in brackets []; [1] denotes the absence of units.

$R = 3,386,200$ [m]: radius of the planet

(x, y) [m]: map coordinates

(L,ϕ) [radian]: longitude (from 0 to 2π), latitude (from $-\frac{\pi}{2}$ to $\frac{\pi}{2}$)

γ [1]: local slope

Q_{sun} [W m^{-2}]: instantaneous absorbed energy from the direct sunlight

Q_{scat} [W m^{-2}]: instantaneous absorbed energy from the sunlight scattered by the atmosphere

Q_{IR} [W m^{-2}]: instantaneous absorbed energy from the thermal emission of the atmosphere

Q_{floor} [W m^{-2}]: instantaneous absorbed energy from the thermal emission of the neighboring facets

$\overrightarrow{r_{surf}}(L, \phi)$ [1]: normalized radius vector of a point at the surface assuming a spherical planet

$\overrightarrow{r_{sun}}(\alpha, \delta)$ [1]: normalized radius vector of the sub-solar point

$\overrightarrow{n_{surf}}(L_n, \phi_n)$ [1]: normalized vector of the direction normal to the local surface

$\Pi_{L_{min}}^{L_{max}}(L)$: door function.

$S_{sun} = 589$ [W m^{-2}]: solar constant at the mean distance between Mars and the Sun $\langle d_{sun} \rangle$

r_{sun} [m]: ratio of mean distance between Mars and the Sun over the distance at time t $\langle d_{sun} \rangle / d_{sun}(t)$. We calculate this distance $d_{sun}(t)$ for any date t using the astronomical parameters determined by the celestial measurements of Pathfinder at J2000 by Allison and McEwen (2000).

A_{vis} [1]: bolometric albedo in the visible. We assume a lambertian surface $A_{dh,vis}(\theta_i) = A_{vis}$ and no dependence on the incidence angle (see Eq. 1).

A_{IR} [1]: bolometric albedo in the thermal infra-red . We assume a lambertian

surface $A_{dh,IR}(\theta_i) = A_{IR}$ and no dependence on the incidence angle. Albedo in the IR is linked to emissivity through $A_{IR} = 1 - \varepsilon$ (Warren et al., 1990).

$f = 0.06$: fraction of light attenuated by the atmosphere. This value was used in the modeling by Kieffer et al., 1977; Aharonson and Schorghofer, 2006. $f \simeq f_{scat} + f_{IR}$

$f_{scat} = 0.02$ [1]: fraction of the direct sunlight scattered by the atmosphere. This value was already used in the modeling by Kieffer et al., 1977; Aharonson and Schorghofer, 2006.

$f_{IR} = 0.04$ [1]: equivalent fraction of noon time direct sunlight emitted by the atmosphere. This value, discussed by Haberle and Jakosky, 1991, was already used in the modeling by Aharonson and Schorghofer, 2006.

$H = 0.8$ [1]: Hurst exponent, describing the topographical roughness.

ε [1]: thermal emissivity (see A_{IR}).

$\sigma = 5.67 * 10^{-8}$ [W m^{-2} K^{-4}]: Stefan Boltzmann constant.

T [K]: temperature of the surrounding soil. This temperature is assumed to be the same as that for the considered facet. If the current facet is frosted and the surrounding ones are defrosted, Q_{floor} is underestimated.

D Summary of the parameters used for modeling the defrost mass balance

In addition to the radiative parameters described in section C, there are the parameters below.

$L_{CO_2} = 590 * 10^3$ [J kg^{-1}]: latent heat for CO_2 sublimation.

T_{surf} [K]: temperature of the facet.

M_{CO_2} [kg m^{-2}]: CO_2 mass of the frost layer.

t [s]: time.

Acknowledgements

This work is supported by a PhD grant from the 'Ministère délégué à l'Enseignement supérieur et à la Recherche' and by a contract with CNES through its 'Système Solaire' program. We thank the OMEGA team at IAS for support with sequencing and data download activities. The authors also would like to thank Nicolas Jourdain for useful discussions and Harvey Harder to improve the English of this article.

References

Aharonson, O., Mar. 2004. Sublimation at the Base of a Seasonal CO_2 Slab on Mars. In: Mackwell, S., Stansbery, E. (Eds.), Lunar Planet. Sci. Conf. pp. 1918–+.

Aharonson, O., Schorghofer, N., Nov. 2006. Subsurface ice on Mars with rough topography. J. Geophys. Res. (E) 111, 11007–+.

Aharonson, O., Zuber, M. T., Rothman, D. H., Oct. 2001. Statistics of Mars' topography from the Mars Orbiter Laser Altimeter: Slopes, correlations, and physical models. J. Geophys. Res. (E) 106, 23723–23736.

Aharonson, O., Zuber, M. T., Smith, D. E., Neumann, G. A., Feldman, W. C., Prettyman, T. H., May 2004. Depth, distribution, and density of CO_2 deposition on Mars. J. Geophys. Res. (E) 109, 5004–+.

Allison, M., McEwen, M., Feb. 2000. A post-Pathfinder evaluation of areocentric solar coordinates with improved timing recipes for Mars seasonal/diurnal climate studies. Planet. Space Sci. 48, 215–235.

Benson, J. L., James, P. B., Apr. 2005. Yearly comparisons of the martian polar caps: 1999-2003 Mars Orbiter Camera observations. Icarus 174, 513–523.

Bintanja, R., 1999. On the glaciological, meteorological, and climatological significance of antarctic blue ice areas. Reviews of Geophysics 37, 337–360.

Brown, G. N. J., Ziegler, W. T., 1979. Vapor pressure and heats of vaporization and sublimation of liquids and solids of interest in cryogenics below 1-atm pressure. Advences in Cryogenic Engineering 25, 662–670.

Campbell, B. A., Ghent, R. R., Shepard, M. K., Feb. 2003. Limits on inference of Mars small-scale topography from MOLA data. Geophys. Res. Lett. 30, 15–1.

Campbell, W. W., Jan. 1895. The Irregular Waning of the South Polar CAP of Mars. Publications of the Astronomical Society of the Pacific 7, 40–+.

Colaprete, A., Barnes, J. R., Haberle, R. M., Hollingsworth, J. L., Kieffer, H. H., Titus, T. N., May 2005. Albedo of the south pole on Mars determined by topographic forcing of atmosphere dynamics. Nature 435, 184–188.

Colaprete, A., Toon, O. B., Jul. 2002. Carbon dioxide snow storms during the polar night on Mars. J. Geophys. Res. (E) 107, 5–1.

Douté, S., Schmidt, F., Schmitt, B., Langevin, Y., Vincendon, M., Bibring, J.-P., Omega Team, Mar. 2008a. Physical Characterization of the South Seasonal Cap of Mars During Recession from OMEGA Observations. Lunar Planet. Sci. Conf. 39, 1736–+.

Douté, S., Schmidt, F., Schmitt, B., Langevin, Y., Vincendon, M., Bibring, J.-P., Omega Team, 2008b. Physical Characterization of the South Seasonal Cap of Mars During Recession from OMEGA Observations. In preparation .

Eluszkiewicz, J., May 1993. On the microphysical state of the martian seasonal caps. Icarus 103 (1), 43–48.

Eluszkiewicz, J., Moncet, J.-L., Dec. 2003. A coupled microphysical/radiative transfer model of albedo and emissivity of planetary surfaces covered by volatile ices. Icarus 166 (2), 375–384.

Forget, F., 1998. Mars CO_2 ice polar caps. In: Schmitt, B., de Bergh, C., Festou, M. (Eds.), Solar System Ices. Vol. 227 of Astrophysics and Space Science Library. Kluwer, pp. 477–507.

Forget, F., Hourdin, F., Fournier, R., Hourdin, C., Talagrand, O., Collins, M., Lewis, S. R., Read, P. L., Huot, J.-P., Oct. 1999. Improved general circulation models of the Martian atmosphere from the surface to above 80 km. J. Geophys. Res. (E) 104, 24155–24176.

Forget, F., Hourdin, F., Talagrand, O., Feb. 1998. CO_2 Snowfall on Mars: Simulation with a General Circulation Model. Icarus 131, 302–316.

Giuranna, M., Grassi, D., Formisano, V., Montabone, L., Forget, F., Zasova, L., Oct. 2008. Pfs/mex observations of the condensing co2 south polar cap of mars. Icarus 197 (2), 386–402.

Haberle, R. M., Jakosky, B. M., Apr. 1991. Atmospheric effects on the remote determination of thermal inertia on Mars. Icarus 90, 187–204.

Hansen, G. B., Sep. 1997. The infrared absorption spectrum of carbon dioxide ice from 1.8 to 333 μm. J. Geophys. Res. (E) 102, 21569–21588.

Hansen, G. B., Jul. 1999. Control of the radiative behavior of the Martian polar caps by surface CO_2 ice: Evidence from Mars Global Surveyor measurements. J. Geophys. Res. (E) 104, 16471–16486.

Hapke, B., 1993. Theory of reflectance and emittance spectroscopy. Topics in Remote Sensing, Cambridge, UK: Cambridge University Press.

Iwasaki, K., Saito, Y., Nakai, Y., Akabane, T., Panjaitan, E., Aug. 1990. Martian south polar CAP 1988. J. Geophys. Res. (E) 95, 14751–14754.

James, P. B., Briggs, G., Barnes, J., Spruck, A., Jun. 1979. Seasonal recession of Mars' south polar CAP as seen by Viking. J. Geophys. Res. (E) 84, 2889–2922.

James, P. B., Cantor, B. A., Davis, S., Oct. 2001. Mars Orbiter Camera observations of the Martian south polar cap in 1999-2000. J. Geophys. Res. (E) 106, 23635–23652.

James, P. B., Cantor, B. A., Malin, M. C., Edgett, K., Carr, M. H., Daniel-

son, G. E., Ingersoll, A. P., Davies, M. E., Hartmann, W. K., McEwen, A. S., Soderblom, L. A., Thomas, P. C., Veverka, J., Apr. 2000. The 1997 Spring Regression of the Martian South Polar Cap: Mars Orbiter Camera Observations. Icarus 144, 410–418.

Kelly, N. J., Boynton, W. V., Kerry, K., Hamara, D., Janes, D., Reedy, R. C., Kim, K. J., Haberle, R. M., Dec. 2006. Seasonal polar carbon dioxide frost on Mars: CO_2 mass and columnar thickness distribution. J. Geophys. Res. (E) 111, 3–+.

Kieffer, H. H., Christensen, P. R., Titus, T. N., Aug. 2006. Co_2 jets formed by sublimation beneath translucent slab ice in mars' seasonal south polar ice cap. Nature 442 (7104), 793–796.

Kieffer, H. H., Martin, T. Z., Peterfreund, A. R., Jakosky, B. M., Miner, E. D., Palluconi, F. D., Sep. 1977. Thermal and albedo mapping of Mars during the Viking primary mission. J. Geophys. Res. (E) 82, 4249–4291.

Kieffer, H. H., Titus, T. N., Mullins, K. F., Christensen, P. R., Apr. 2000. Mars south polar spring and summer behavior observed by TES: Seasonal cap evolution controlled by frost grain size. J. Geophys. Res. (E) 105, 9653–9700.

Langevin, Y., Bibring, J.-P., Montmessin, F., Forget, F., Vincendon, M., Douté, S., Poulet, F., Gondet, B., Jul. 2007. Observations of the south seasonal cap of Mars during recession in 2004-2006 by the OMEGA visible/near-infrared imaging spectrometer on board Mars Express. J. Geophys. Res. (E) 112, 8–+.

Langevin, Y., Douté, S., Vincendon, M., Poulet, F., Bibring, J.-P., Gondet, B., Schmitt, B., Forget, F., Aug. 2006. No signature of clear co_2 ice from the 'cryptic' regions in mars' south seasonal polar cap. Nature 442 (7104), 790–792.

Laskar, J., Joutel, F., Boudin, F., Mar. 1993. Orbital, precessional, and insolation quantities for the Earth from -20 Myr to +10 Myr. Astron. and Astrophys. 270, 522–533.

Leighton, R. R., Murray, B. C., Jul. 1966. Behavior of carbon dioxide and other volatiles on Mars. Science 153, 136–144.

Lewis, S. R., Collins, M., Read, P. L., Forget, F., Hourdin, F., Fournier, R., Hourdin, C., Talagrand, O., Huot, J.-P., Oct. 1999. A climate database for Mars. J. Geophys. Res. (E) 104, 24177–24194.

Litvak, M. L., Mitrofanov, I. G., Kozyrev, A. S., Sanin, A. B., Tretyakov, V. I., Boynton, W. V., Kelly, N. J., Hamara, D., Saunders, R. S., Feb. 2007. Long-term observations of southern winters on Mars: Estimations of column thickness, mass, and volume density of the seasonal CO_2 deposit from HEND/Odyssey data. J. Geophys. Res. (E) 112, 3–+.

Malamud, B. D., Turcotte, D. L., Aug. 2001. Wavelet analyses of Mars polar topography. J. Geophys. Res. (E) 106, 17497–17504.

Murchie, S. L., and 42 colleagues, Dec. 2004. CRISM (Compact Reconnaissance Imaging Spectrometer for Mars) on MRO (Mars Reconnaissance Orbiter). In: Nardell, C. A., Lucey, P. G., Yee, J.-H., Garvin, J. B. (Eds.), Ap-

plications with Weather Satellites II. Edited by Menzel, W. Paul; Iwasaki, Toshiki. Proceedings of the SPIE, Volume 5660, pp. 66-77 (2004). pp. 66–77.

Paige, D. A., Ingersoll, A. P., Jun. 1985. Annual heat balance of Martian polar caps - Viking observations. Science 228, 1160–1168.

Piqueux, S., Byrne, S., Richardson, M. I., Aug. 2003. Sublimation of Mars's southern seasonal CO_2 ice cap and the formation of spiders. J. Geophys. Res. (E) 108, 3–1.

Pollack, J. B., Haberle, R. M., Schaeffer, J., Lee, H., Feb. 1990. Simulations of the general circulation of the Martian atmosphere. I - Polar processes. J. Geophys. Res. (E) 95, 1447–1473.

Portyankina, G., Markiewicz, W. J., Oct. 2003. Model for Formation of Spider Patterns in the Cryptic Region. In: Clifford, S., Doran, P., Fisher, D., Herd, C. (Eds.), Third International Conference on Mars Polar Science and Exploration. pp. 8026–+.

Press, W. H., Flannery, B. P., Teukolsky, S. A., Vetterling, W. T., 1986-1992. Numerical Recipes in Fortran 77 : the art of scientific computing. Cambridge University Press, Ch. 4.4, pp. 110–114.

Putzig, N. E., Mellon, M. T., Kretke, K. A., Arvidson, R. E., Feb. 2005. Global thermal inertia and surface properties of Mars from the MGS mapping mission. Icarus 173, 325–341.

Sayles, R. S., Thomas, T. R., Feb. 1978. Surface topography as a nonstationary random process. Nature 271 (5644), 431–434.

Schmidt, F., Douté, S., Schmitt, B., 2007. Wavanglet: An efficient supervised classifier for hyperspectral images. Geoscience and Remote Sensing, IEEE Transactions on 45 (5), 1374–1385.

Schmitt, B., Quirico, E., Trotta, F., Grundy, W. M., 1998. Optical Properties of Ices from UV to Infrared. In: Schmitt, B., de Bergh, C., Festou, M. (Eds.), Solar System Ices. Vol. 227 of Astrophysics and Space Science Library. Kluwer, pp. 199–240.

Schmitt, B., Schmidt, F., Douté, S., Langevin, Y., Forget, F., Bibring, J.-P., Gondet, B., Omega Team, Oct. 2006. Recession of the Northern Seasonal Condensates on Mars by OMEGA/Mars Express. LPI Contributions 1323, 8050–+.

Schorghofer, N., Aharonson, O., May 2005. Stability and exchange of subsurface ice on Mars. J. Geophys. Res. (E) 110, 5003–+.

Shchuko, O. B., Kartashov, D. V., Picardi, G., Orosei, R., Jan. 2003. Martian underground water detection: Thermal model and simulations of radar signal propagation. J. Geophys. Res. (E) 108, 3–1.

Shepard, M. K., Campbell, B. A., Aug. 1998. Shadows on a Planetary Surface and Implications for Photometric Roughness. Icarus 134, 279–291.

Shepard, M. K., Campbell, B. A., Bulmer, M. H., Farr, T. G., Gaddis, L. R., Plaut, J. J., Dec. 2001. The roughness of natural terrain: A planetary and remote sensing perspective. J. Geophys. Res. (E) 106, 32777–32796.

Thomas, P., Veverka, J., Campos-Marquetti, R., Aug. 1979. Frost streaks in the south polar CAP of Mars. J. Geophys. Res. (E) 84, 4621–4633.

Titus, T. N., Mar. 2005. Mars Polar Cap Edges Tracked over 3 Full Mars Years. In: Mackwell, S., Stansbery, E. (Eds.), 36th Annual Lunar and Planetary Science Conference. pp. 1993–+.

Veverka, J., Goguen, J., Dec. 1973. The Nonuniform Recession of the South Polar Cap of Mars. Journal of the Royal Astronomical Society of Canada 67, 273–+.

Vincendon, M., Langevin, Y., Poulet, F., Bibring, J.-P., Gondet, B., Jouglet, D., the OMEGA Team, 2008. Dust aerosols above the south polar cap of mars as seen by omega. Icarus (in press) .

Warren, S. G., Wiscombe, W. J., Firestone, J. F., Aug. 1990. Spectral albedo and emissivity of CO_2 in Martian polar caps - Model results. J. Geophys. Res. (E) 95, 14717–14741.

Latitude (°S)	55	65	75	85
Altitude cryptic sector (m)	1000	1000	2000	2500
Altitude anti-cryptic sector (m)	1000	1000	2000	3500

Table 1
Reference altitudes for both the cryptic and anti-cryptic sectors.

Altitude (m)	-6000	0	**1000**	2000
Defrost mass ($\mathrm{kg\,m^{-2}}$)	107	152	159	166

Table 2
Altitude effect on defrost mass balance at latitude 55°S. The defrost mass model is used for the SSPC anti-cryptic sector recession with the time independent albedo scenario (model M2) discussed in section 4.1.8.

Altitude (m)	1500	**2500**	3500
Defrost mass ($\mathrm{kg\,m^{-2}}$)	1214	1201	1189

Table 3
Same as Tab. 2 at latitude 85°S.

	Latitude	55°S	65°S	75°S	85°S
HEND+GRS	Mass [kg m^{-2}] $M^H_{CO_2/tot}(\phi)$	180±40	450±80	750±100	1050±100
-	Sublimation duration [°Ls] $T^H_{beg}(\phi)/-$	140/ -	160/ -	170/ -	180/ -
Model M2	Sublimation duration [°Ls] $T^{M2}_{beg}(L',\phi)/T^O_{end}(L',\phi)$	135/170	165/220	185/245	200/270
-	Equivalent albedo [1] $A^{M2}_{vis}(L',\phi)$	0.25	0.43	0.43	0.53
-	Min/Max equ. albedo [1] $A^{M2}_{vis}(L',\phi)$	0.17/0.32	0.50/0.37	0.49/0.37	0.57/0.50
Model M3	Mass [kg m^{-2}] $M^{M3}_{CO_2/tot}(L',\phi)$	176	513	715	1118
-	Sublimation duration [°Ls] $T^{M3}_{beg}(L',\phi)/T^O_{end}(L',\phi)$	135/170	160/220	180/245	195/270
Model M1(I=20)	Subsurface heat [kg m^{-2}]	0.5	0.5	0.6	0.6
-	Sublimation duration [°Ls] $T^H_{beg}(\phi)/T^{M1}_{end}(L',\phi)$	140/185	160/235	170/260	180/280
Model M1(I=1000)	Subsurface heat [kg m^{-2}]	12	24	29	21
-	Sublimation duration [°Ls] $T^H_{beg}(\phi)/T^{M1}_{end}(L',\phi)$	140/155	160/215	170/245	180/265

Table 4
Models for the SSPC recession in the cryptic sector. The first two lines are the measurements by HEND/GRS. The next three lines summarize the results of the time independent albedo scenario (model M2). The next two lines summarize the latitude independent albedo scenario (model M3). The last four lines show the heat released by the annual heat wave (model M1) as presented in section 4.1.3.

	Latitude	55°S	65°S	75°S	85°S
HEND+GRS	Mass [kg m^{-2}] $M^{H}_{CO_2/tot}(\phi)$	180±40	450±80	750±100	1050±100
-	Sublimation duration [°Ls] $T^{H}_{beg}(\phi)/-$	140/-	160/-	170/-	180/-
Model M2	Sublimation duration [°Ls] $T^{M2}_{beg}(L',\phi)/T^{O}_{end}(L',\phi)$	135/170	170/225	190/260	205/290
-	Equivalent albedo [1] $A^{M2}_{vis}(L',\phi)$	0.25	0.5	0.59	0.65
-	Min/Max equ. albedo [1] $A^{M2}_{vis}(L',\phi)$	0.17/0.33	0.44/0.56	0.55/0.63	0.63/0.68
Model M3	Mass [kg m^{-2}] $M^{M3}_{CO_2/tot}(L',\phi)$	159	449	743	947
-	Sublimation duration [°Ls] $T^{M3}_{beg}(L',\phi)/T^{O}_{end}(L',\phi)$	135/170	165/225	185/260	205/290
Model M1(I=20)	Subsurface heat [kg m^{-2}]	0.5	0.6	0.7	0.5
-	Sublimation duration [°Ls] $T^{H}_{beg}(\phi)/T^{M1}_{end}(L',\phi)$	140/185	160/245	170/280	180/315
Model M1(I=1000)	Subsurface heat [kg m^{-2}]	12	27	29	27
-	Sublimation duration [°Ls] $T^{H}_{beg}(\phi)/T^{M1}_{end}(L',\phi)$	140/155	160/215	170/245	180/265

Table 5
Same as Tab. 4, but for the SSPC recession models in the anti-cryptic sector.

Tables

Figure captions Fig 1. Structure of the SSPC edge, definition of the inner/outer crocus lines and the snowdrop distance.

Fig 2. Definition of the snowdrop distance at Ls=222.19° for two extreme cases: (a) meridian profile in the cryptic sector (longitude range 115°E-125°E) where the transition zone of CO_2 ice coverage is wide and chaotic, and (b) meridian profile in the anti-cryptic sector (longitude range 195°E-305°E) where the transition zone of CO_2 ice coverage is regular and narrow.

Fig 3. Empirical relation between the reflectance $R^O_{1.07}$ measured by OMEGA at 1.07 microns and the bolometric albedo A^O_{vis} calculated (see eq. 2). The points represent the population of spectra of the observation ORB17886_1. We can find a regression line that fits the cloud of points with a chi-square of 1.41096. The same relation has been found for the observation ORB1868_1.

Fig 4. SSPC recession for both the cryptic (between longitude 60°E and 260°E) and the anti-cryptic sectors (between longitude 100°W and 60°E.). Small cross symbols represent the crocus line points respectively determined by OMEGA using our algorithm (+and×) (see section 2.3) and by TES (∗) (Titus, 2005). Large symbols represent the average position of the OMEGA crocus line for four reference latitudes.

Fig 5. Topography of the SSPC region expressed as a series of MOLA meridian profiles, each with its own color representing the longitude (see Appendix A).

Fig 6. SSPC crocus line points (+and×symbols) for one meridian profile of the cryptic sector (140°-150°E) and one for the anti-cryptic sector (270°-280E) compared to the spatio-temporal pattern of the mean daily absorbed radiation W (gray scale) for an albedo of 0.

Fig 7. SSPC crocus line points (+and× symbols) compared to the spatio-temporal pattern of mean local albedo A^O_{vis} (grey scale) for two meridian profiles, the cryptic (140°-150°E) and anti-cryptic (270°-280E) sectors.

Fig 8. Evaluation of the time independent scenario (model M2) for both cryptic and anti-cryptic sectors. Diamonds are equivalent albedo $A^{M2}_{vis}(L', \phi)$ required to sublimate the frost observed by HEND and GRS. Errors bars are due to the CO_2 thickness measurement uncertainties. Crosses are time averaged albedo $A^{B2}_{vis}(L', \phi)$ of CO_2 (gray scale represents the longitude) measured by OMEGA.

Fig 9. Empirical law of albedo for the latitude independent scenario (model M3) for both cryptic and anti-cryptic sectors. The "+" symbols are latitude averaged albedo $A^{B3}_{vis}(L', Ls)$ of CO_2 ice (gray scale represents the longitude) measured by OMEGA. The dotted line is the empirical fit $A^{M3}_{vis}(L', Ls)$.

Fig 10. SSPC recession compared to local radiation modulated by surface

roughness for two meridian profiles in the longitude ranges (a) 260°-270°E and (b) 270°-280°E. Symbols +and× represent the outer and inner crocus lines respectively. The gray scale represent the statistical index $\hat{P_{stat}}$ (Eq. 20) calculated for the local absorbed radiation W with a special configuration that maximizes the effect of surface roughness (see text).

Fig 11. SSPC recession compared to the albedo distribution observed by OMEGA for six meridian profiles in the longitude ranges (a) 0°-10°E, (b) 70°-80°E, (c) 200°-210°E, (d) 260°-270°E, (e) 270°-280°E and (f) 320°-330°E. Symbols +and× represent the outer and inner crocus lines respectively. The gray scale represents the statistical index $\hat{P_{stat}}$ (Eq. 20) calculated for the local absorption factor Abs_{vis}^{O} inside each bin.

Fig 12. Scatterplot generated to test the correlation between the snowdrop time and the statistical index $\hat{P_{stat}}$calculated for the albedo, for all longitude ranges. Albedo is taken to be 22.5 to 18.5°Ls before the inner crocus date.

Fig 13. SSPC recession compared to the sublimated CO_2 mass distribution computed for six meridian profiles in the longitude ranges (a) 0°-10°E, (b) 70°-80°E, (c) 200°-210°E, (d) 260°-270°E, (e) 270°-280°E and (f) 320°-330°E. Symbols +and× represent the outer and inner crocus lines respectively. The gray scale represents the statistical index $\hat{P_{stat}}$ (Eq. 20) calculated for the local daily defrosted mass $\frac{\partial M_{CO_2}}{\partial t}$ inside each bin.

Fig 14. Scatterplot generated to test the correlation between the snowdrop time and the statistical index $\hat{P_{stat}}$calculated for the daily defrost mass with a homogeneous albedo and heterogeneous slopes, for all longitude ranges. The modeled sublimed mass is taken to be 22.5 to 18.5°Ls before the inner crocus date.

Figures

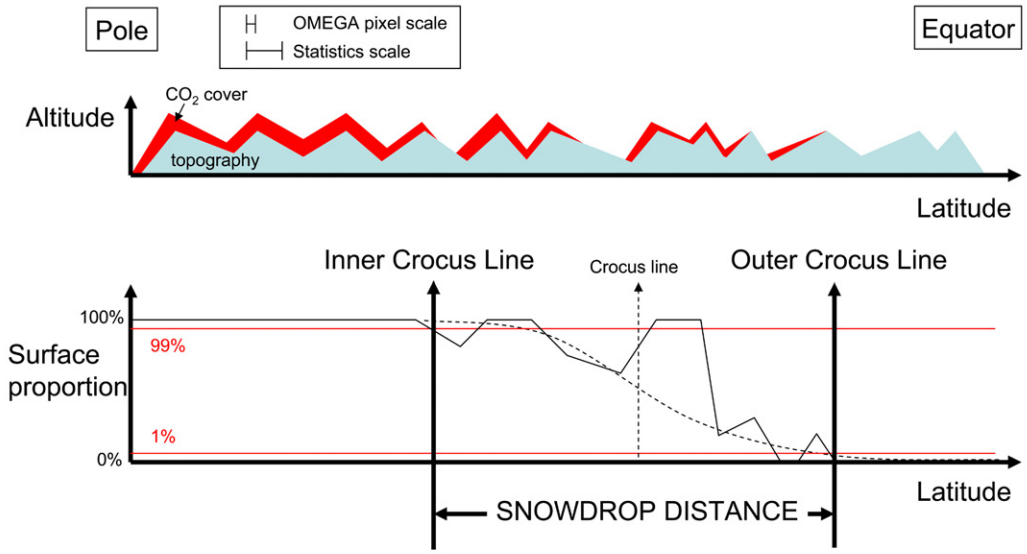

Figure 1.

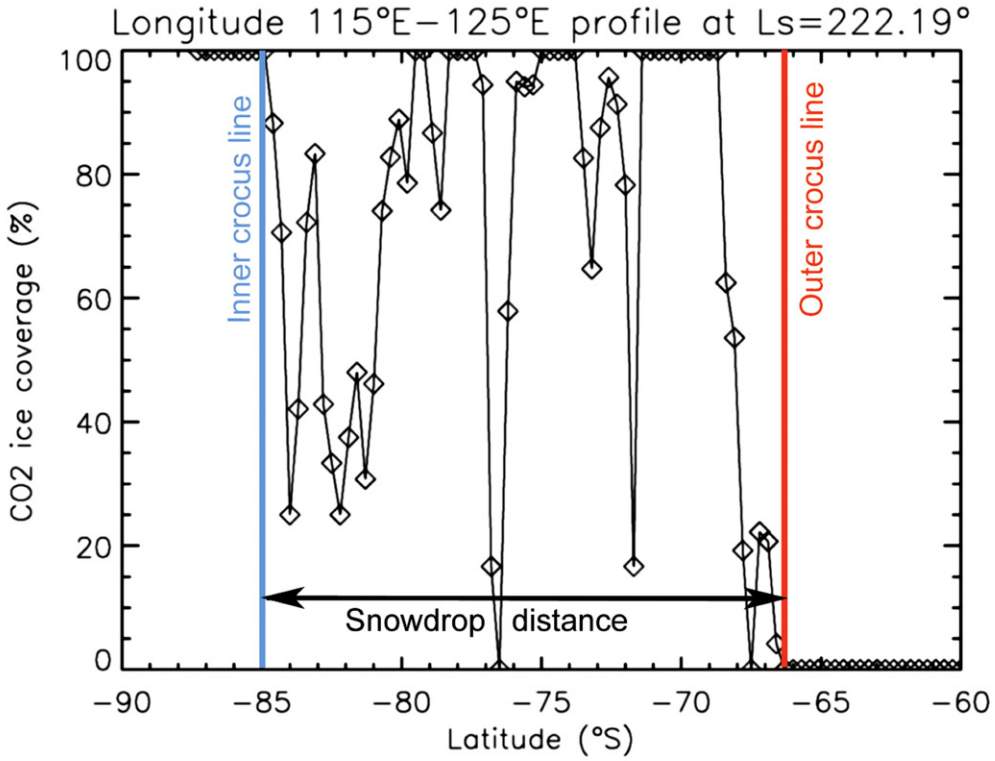

(a) Cryptic sector

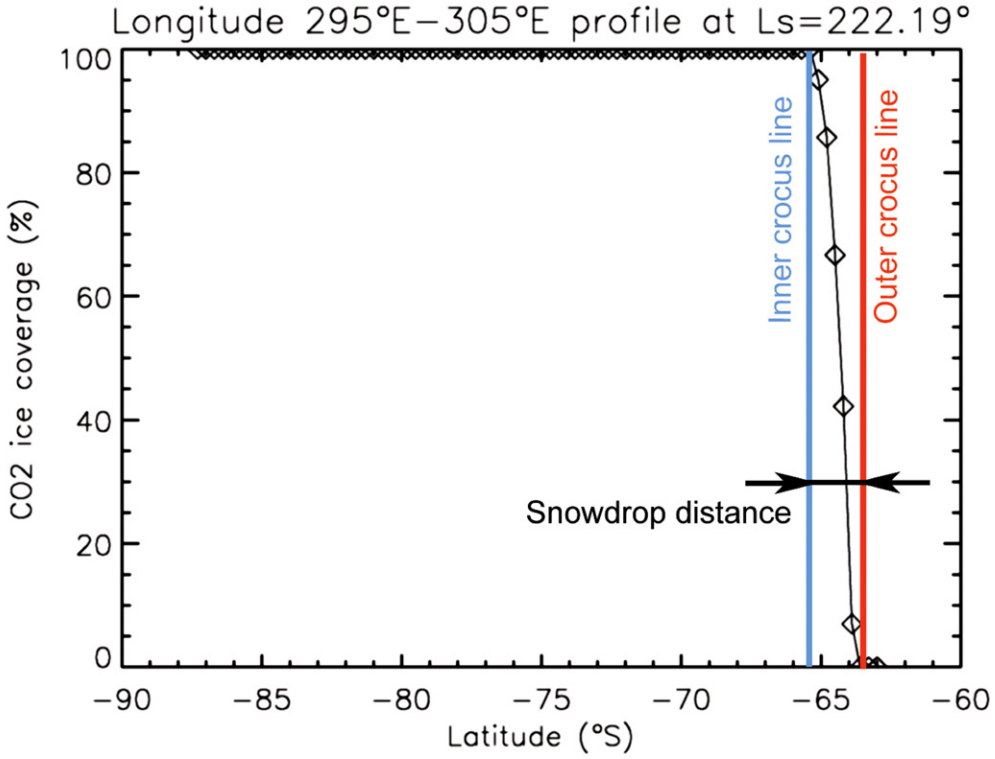

(b) Anticryptic sector

Figure 2.

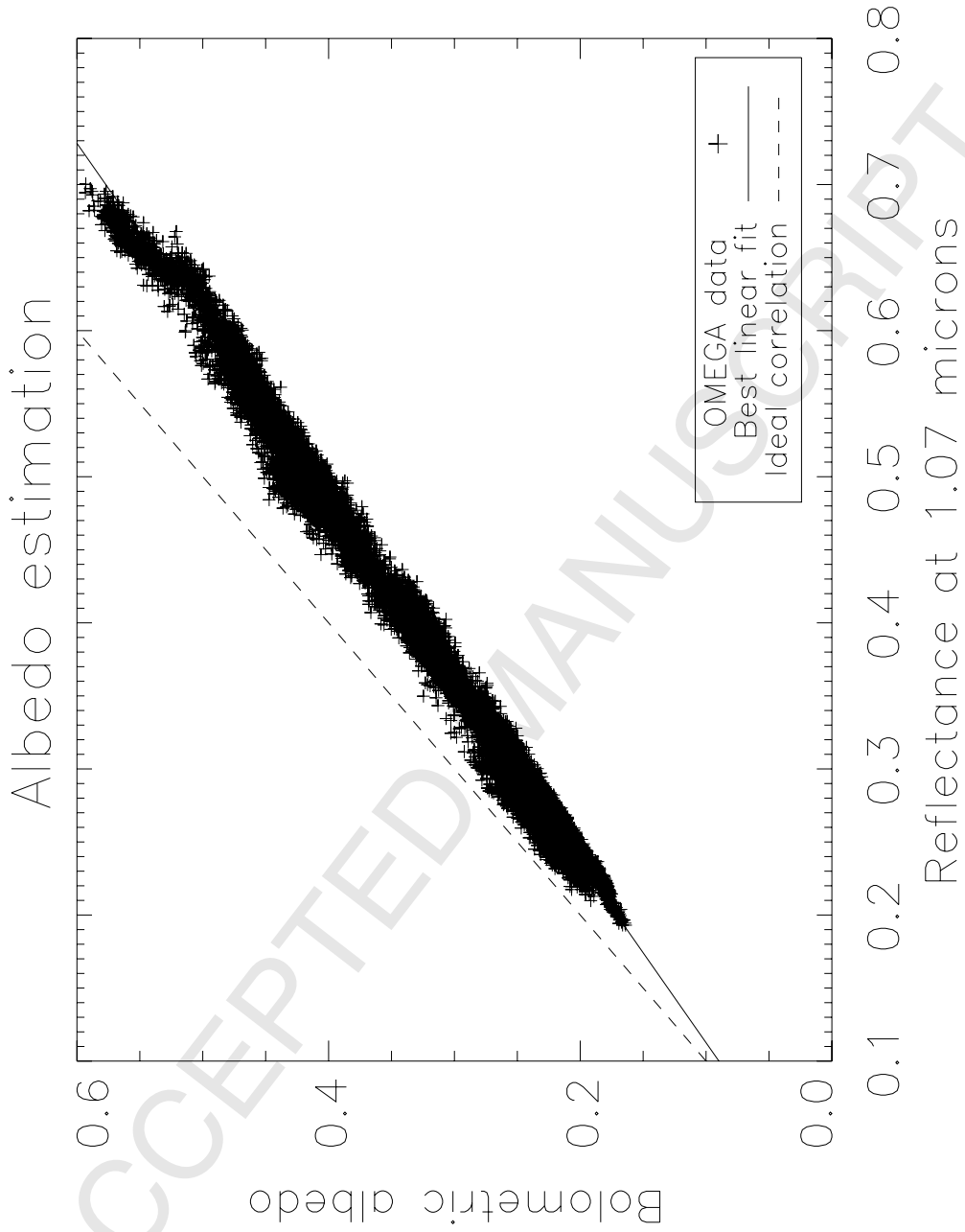

Figure 3.

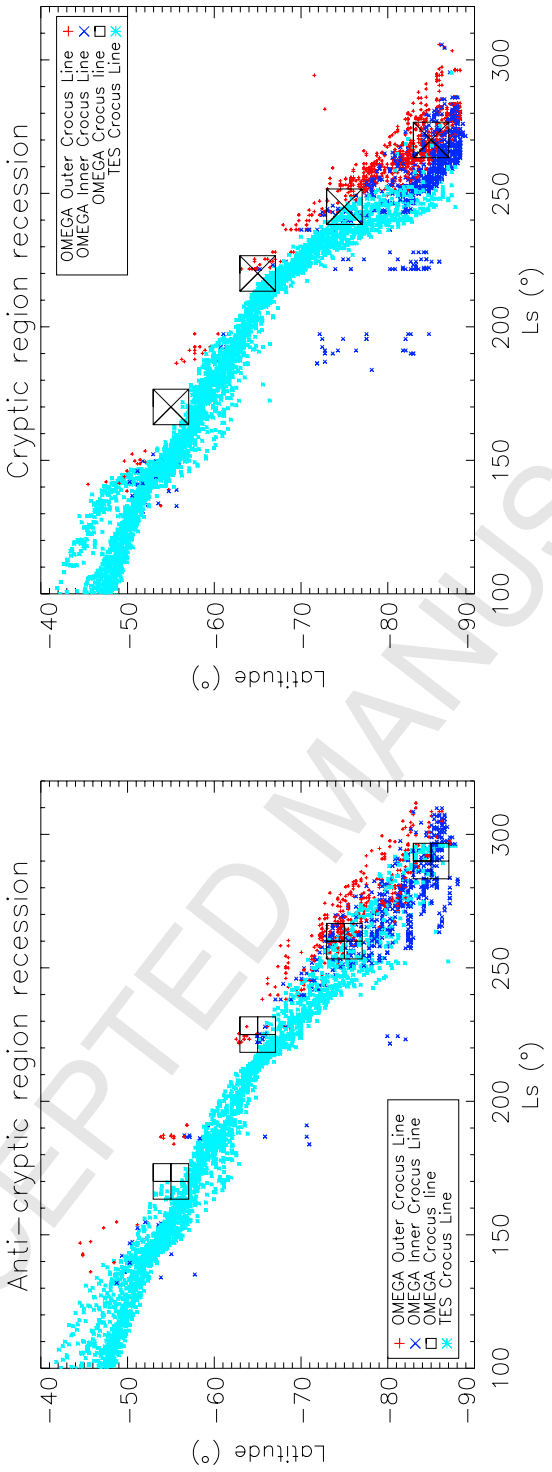

Figure 4.

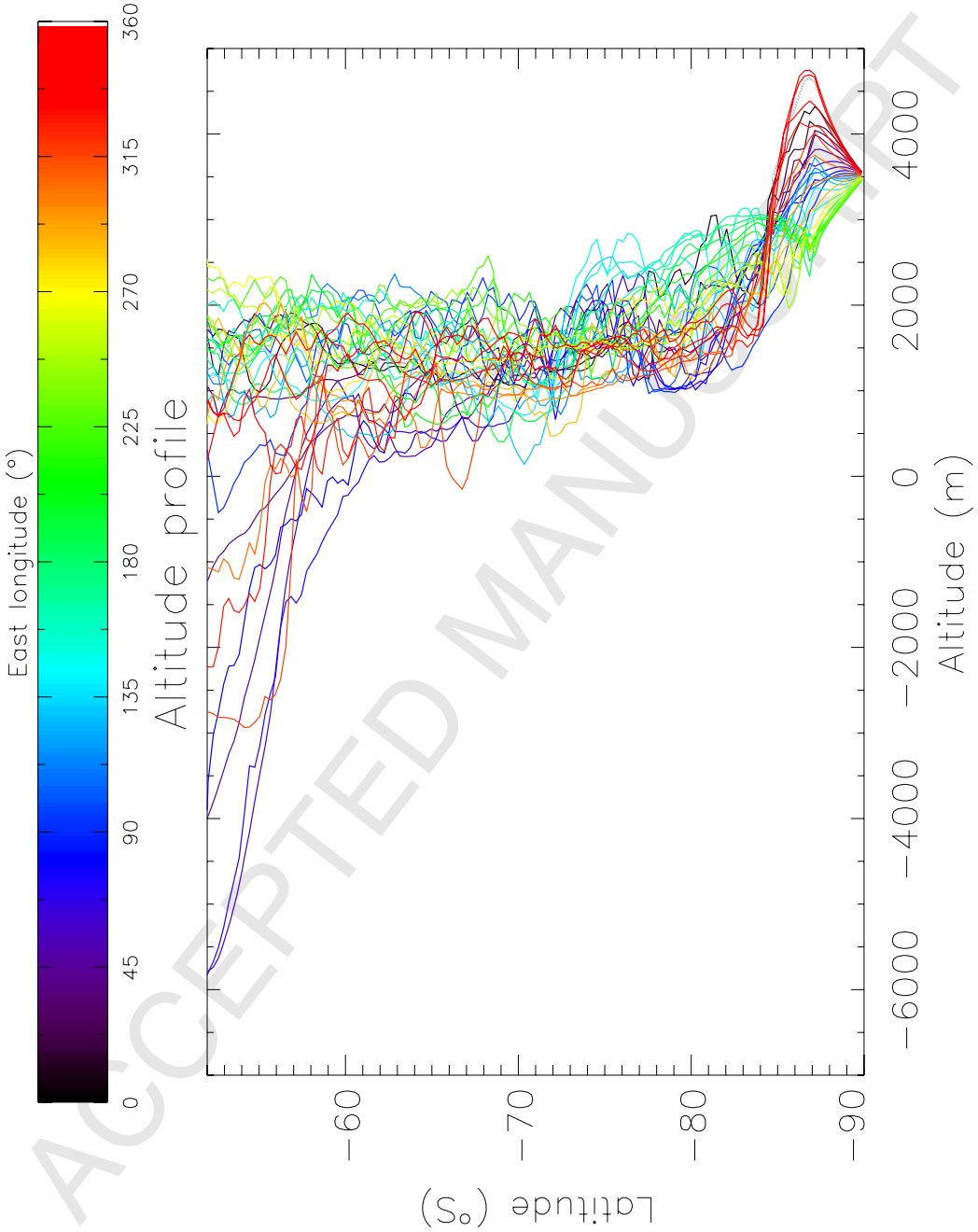

Figure 5.

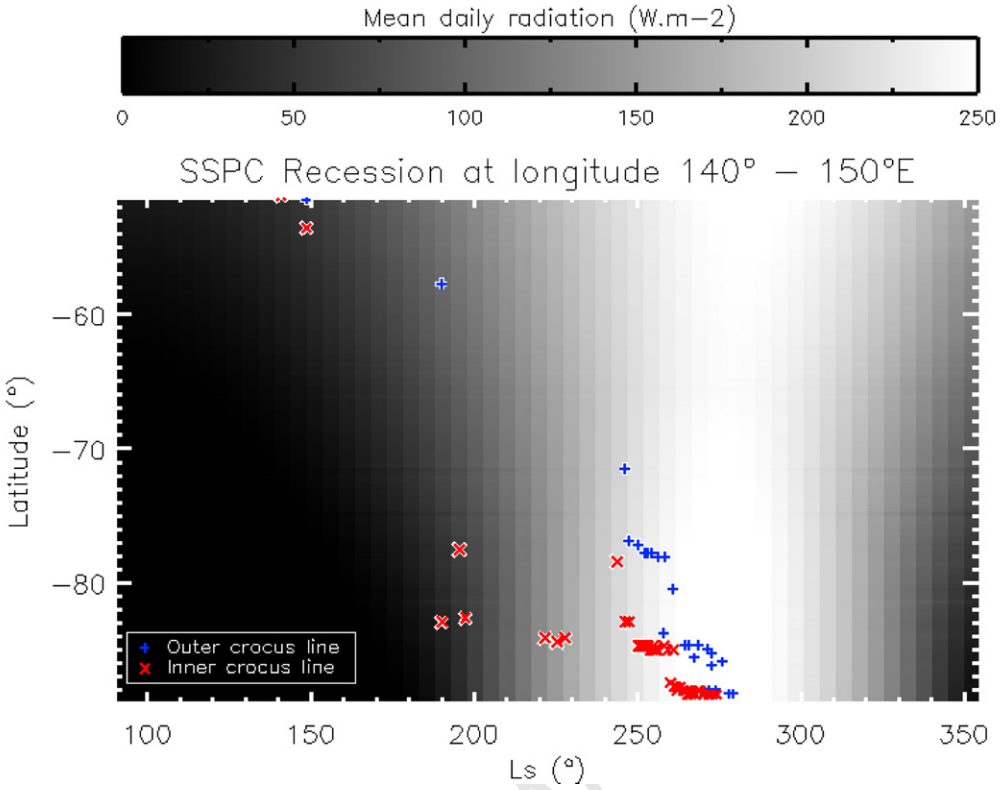

(a)

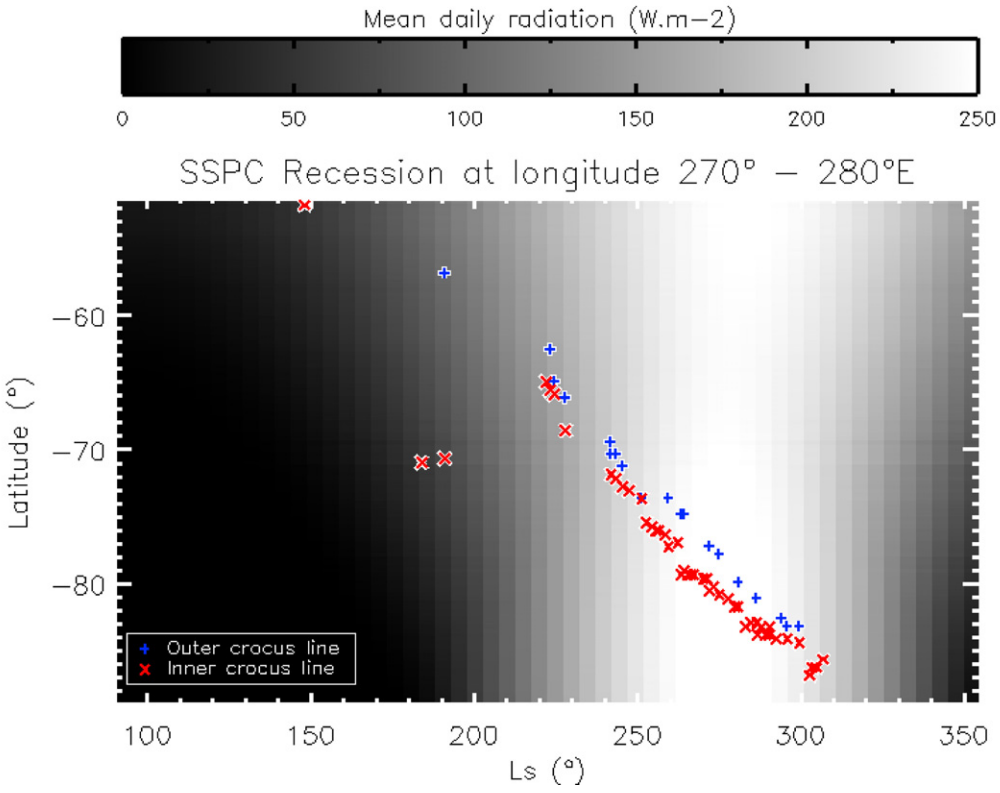

(b)

Figure 6.

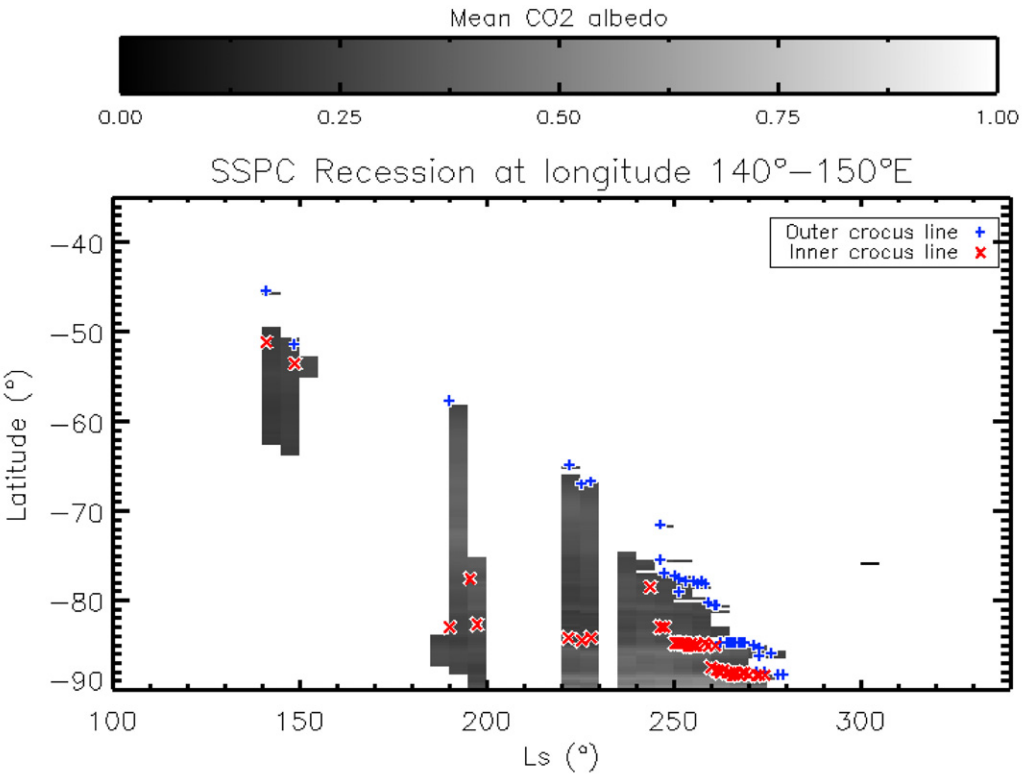

(a)

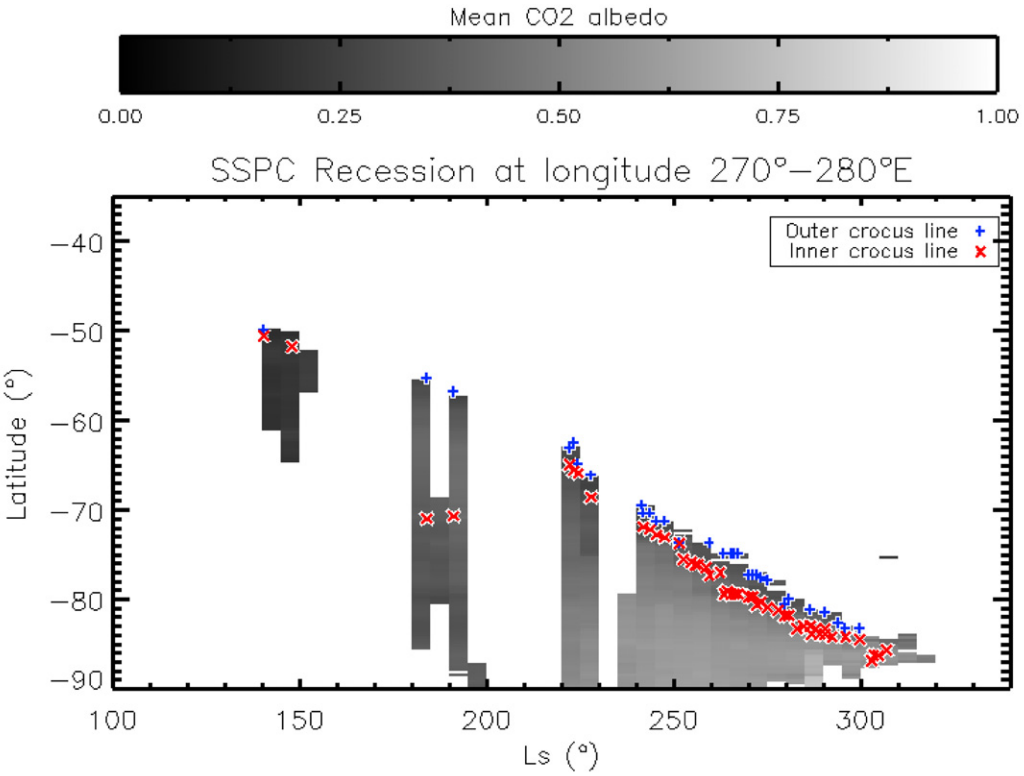

(b)

Figure 7.

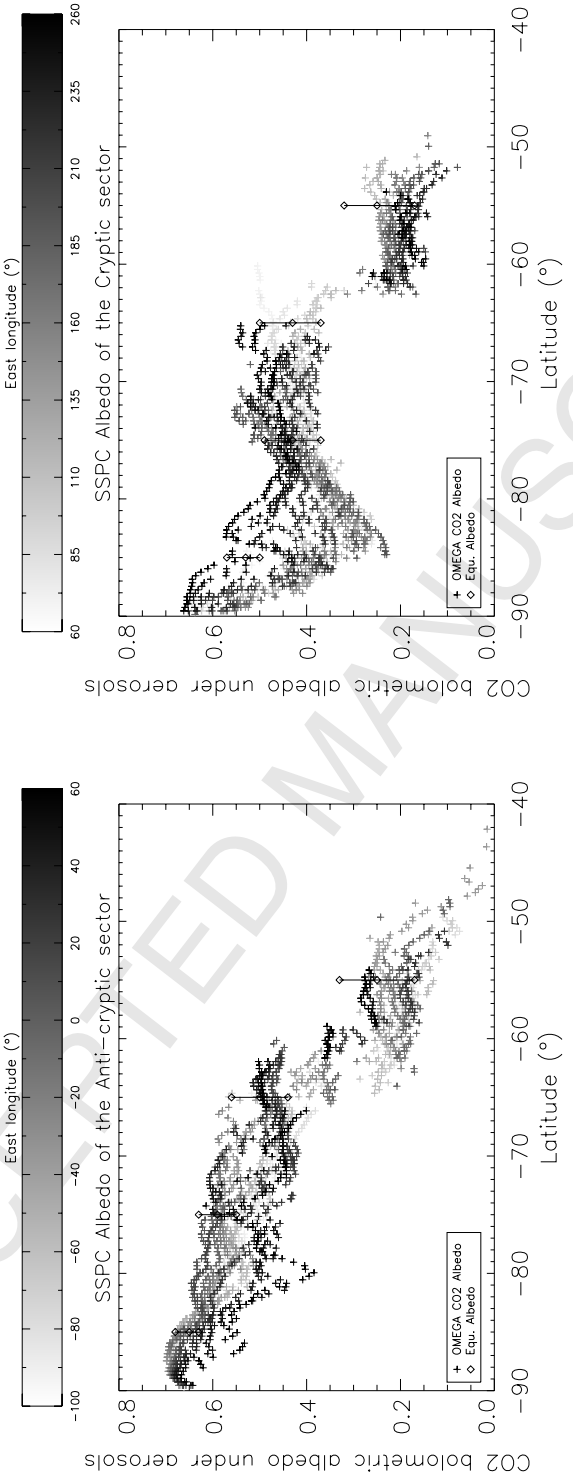

Figure 8.

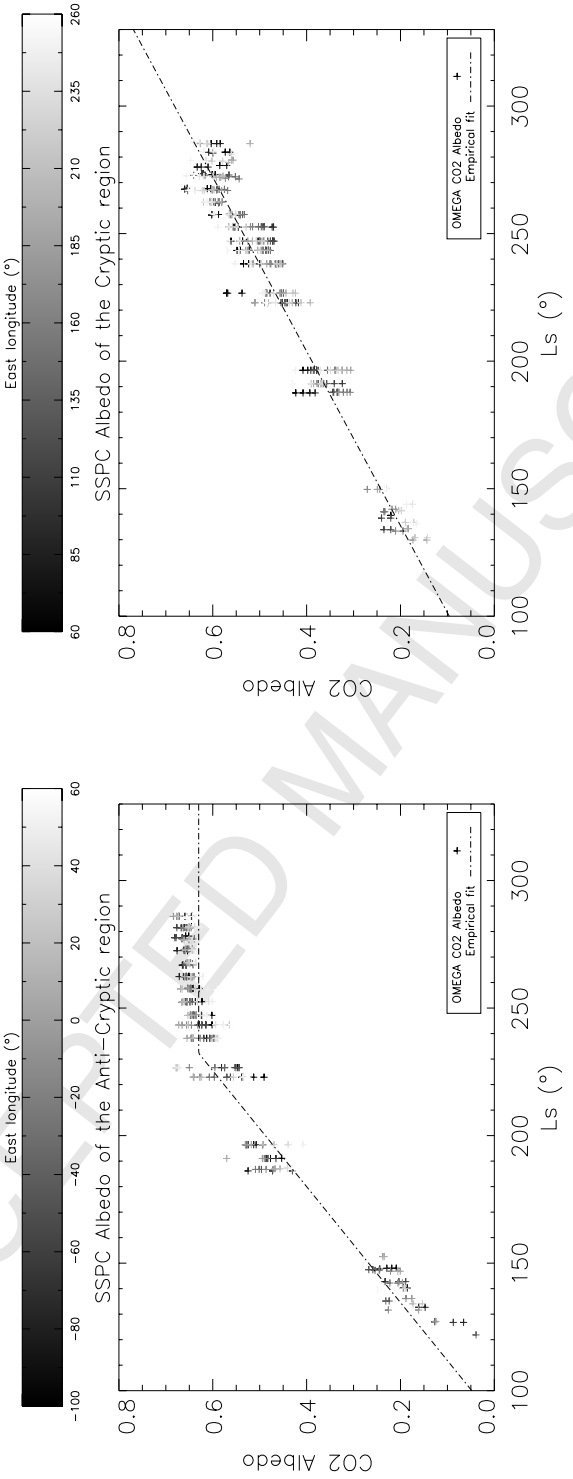

Figure 9.

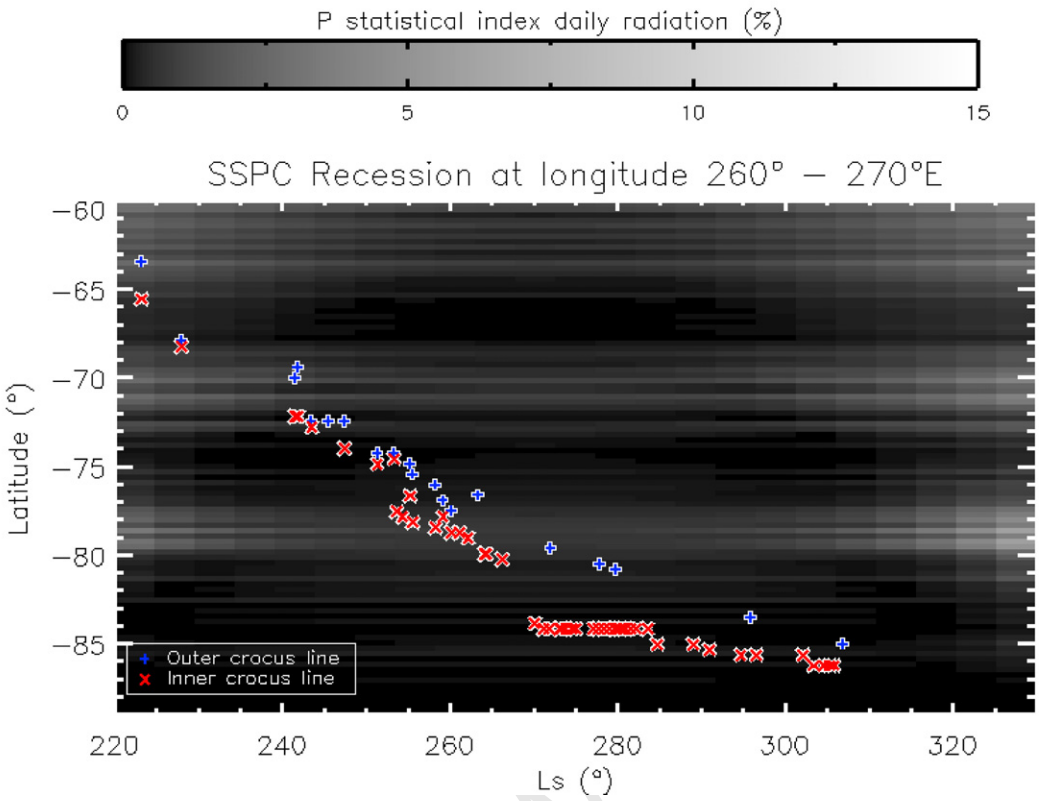

(a)

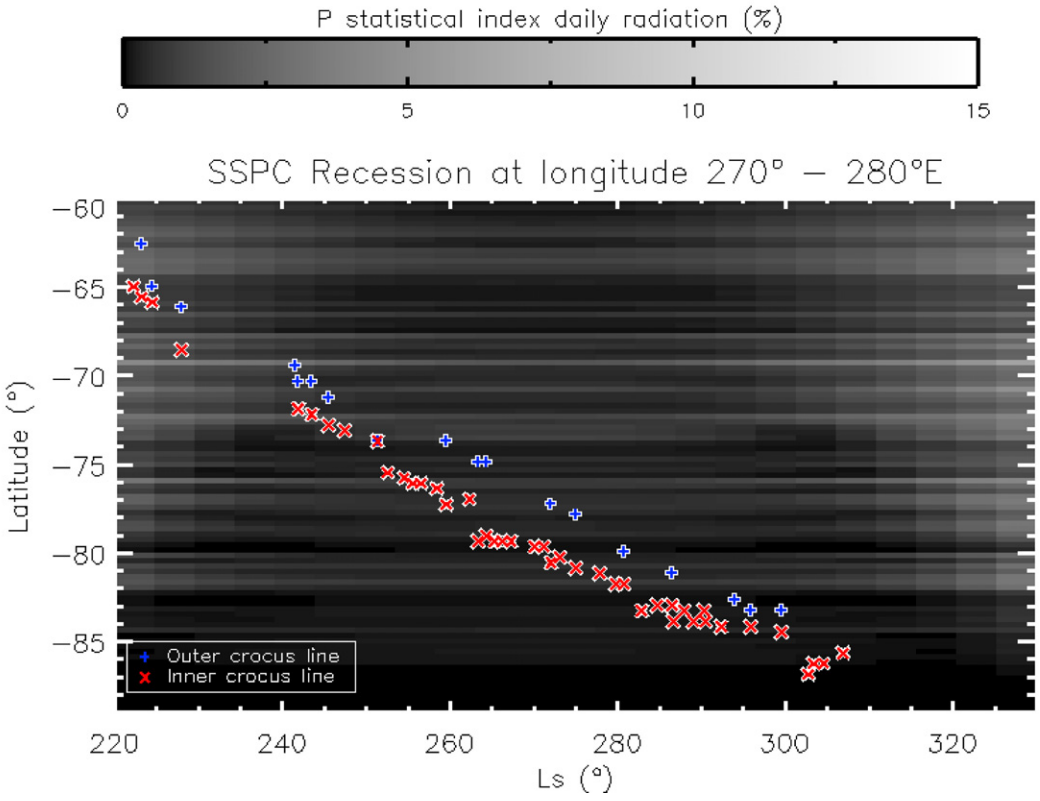

61 (b)

Figure 10.

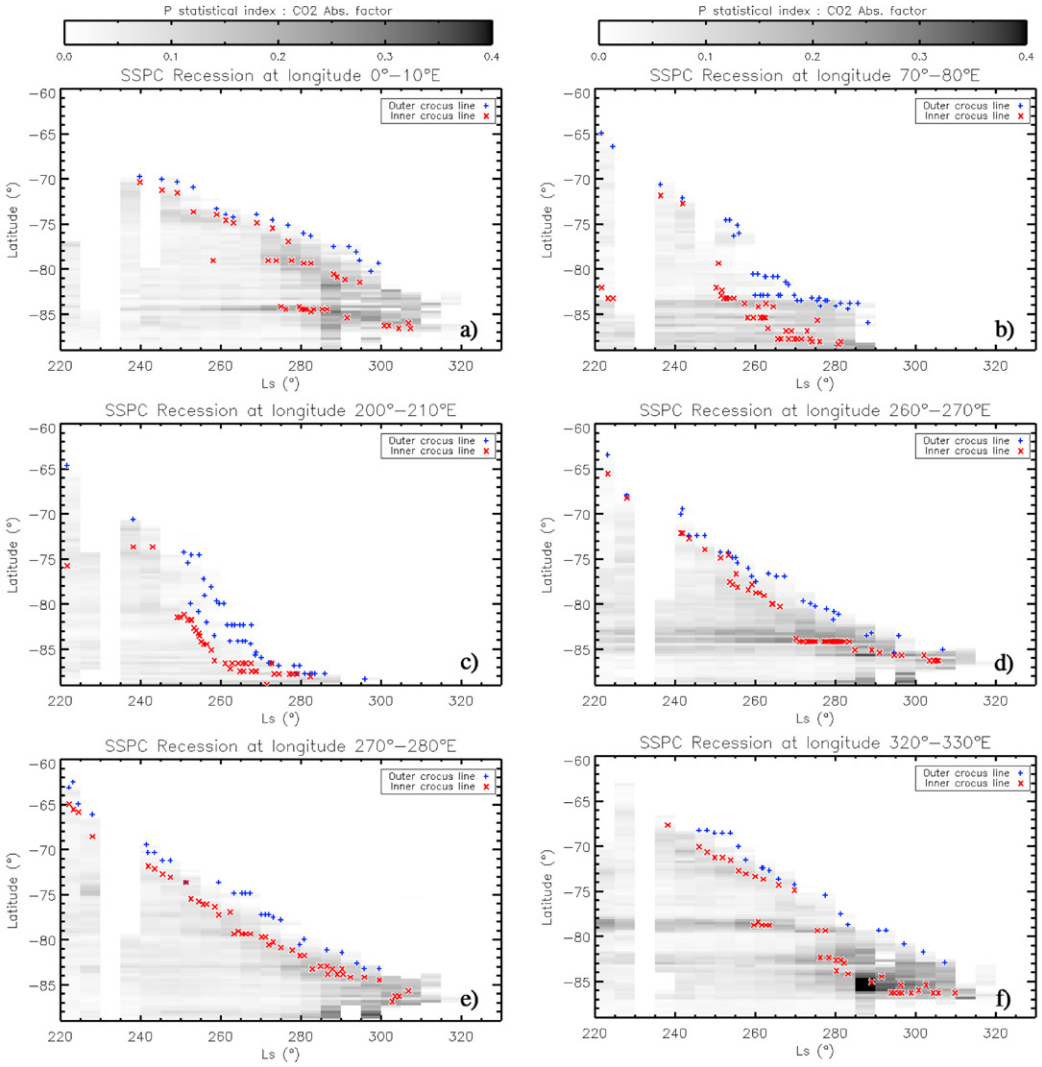

Figure 11.

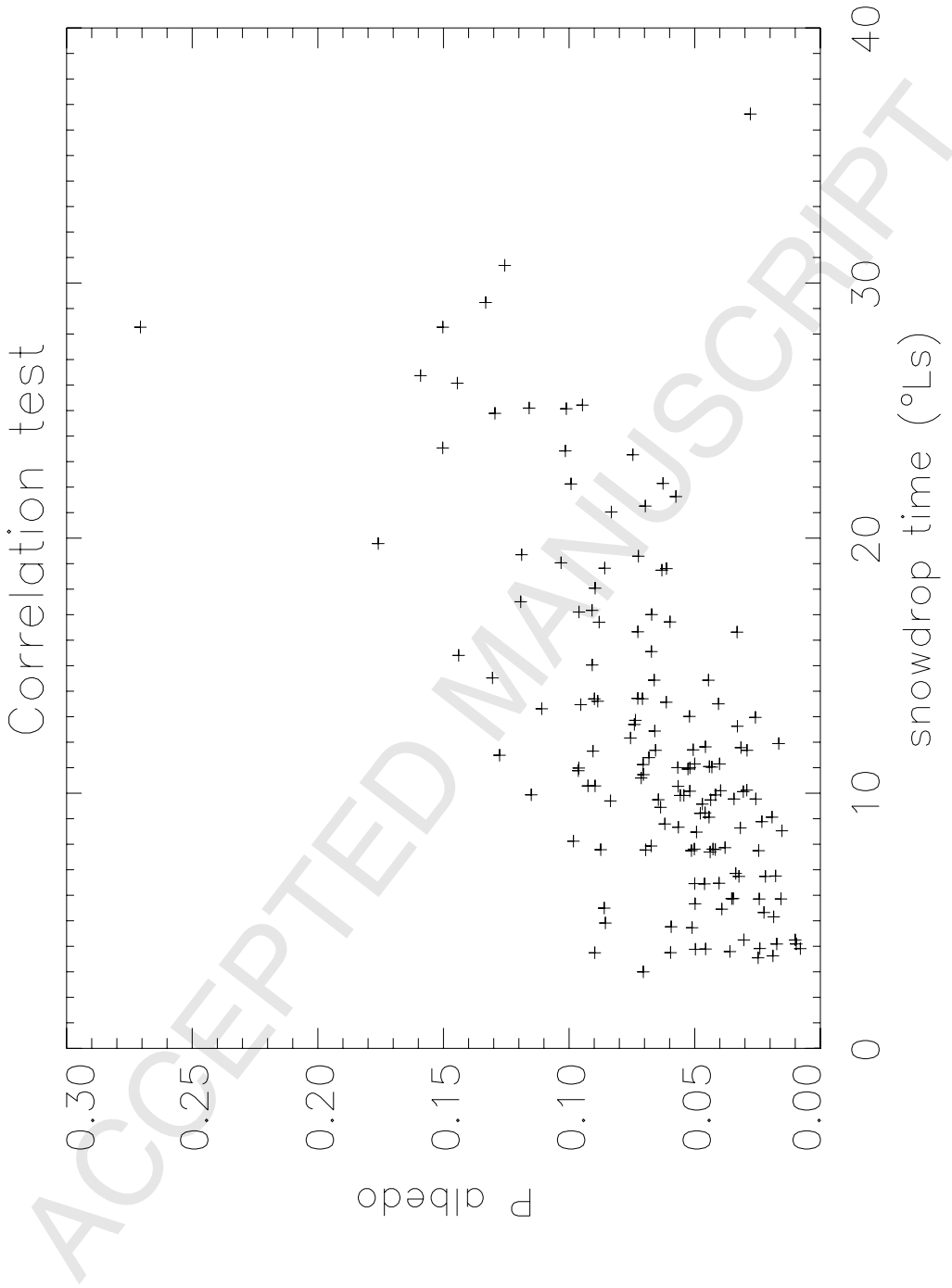

Figure 12.

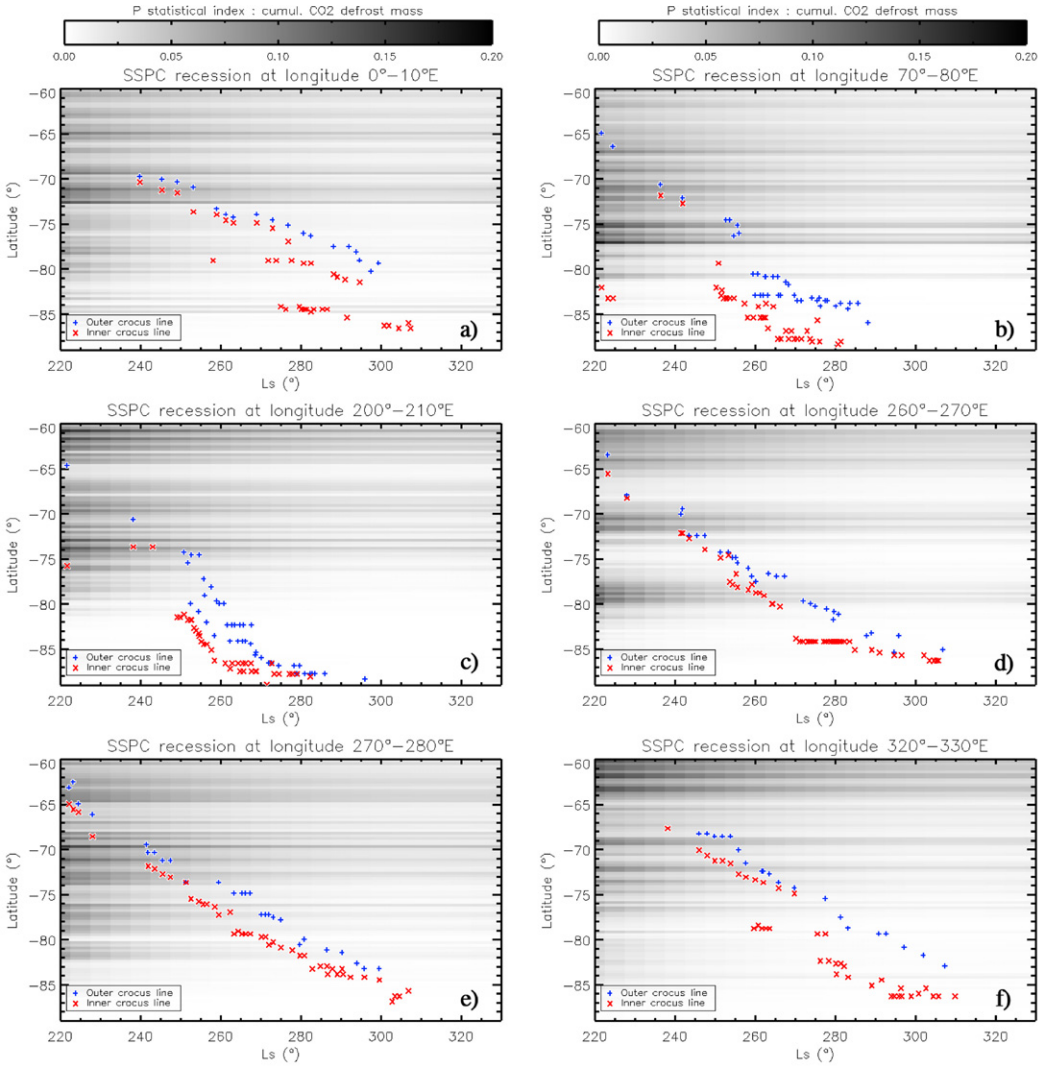

Figure 13.

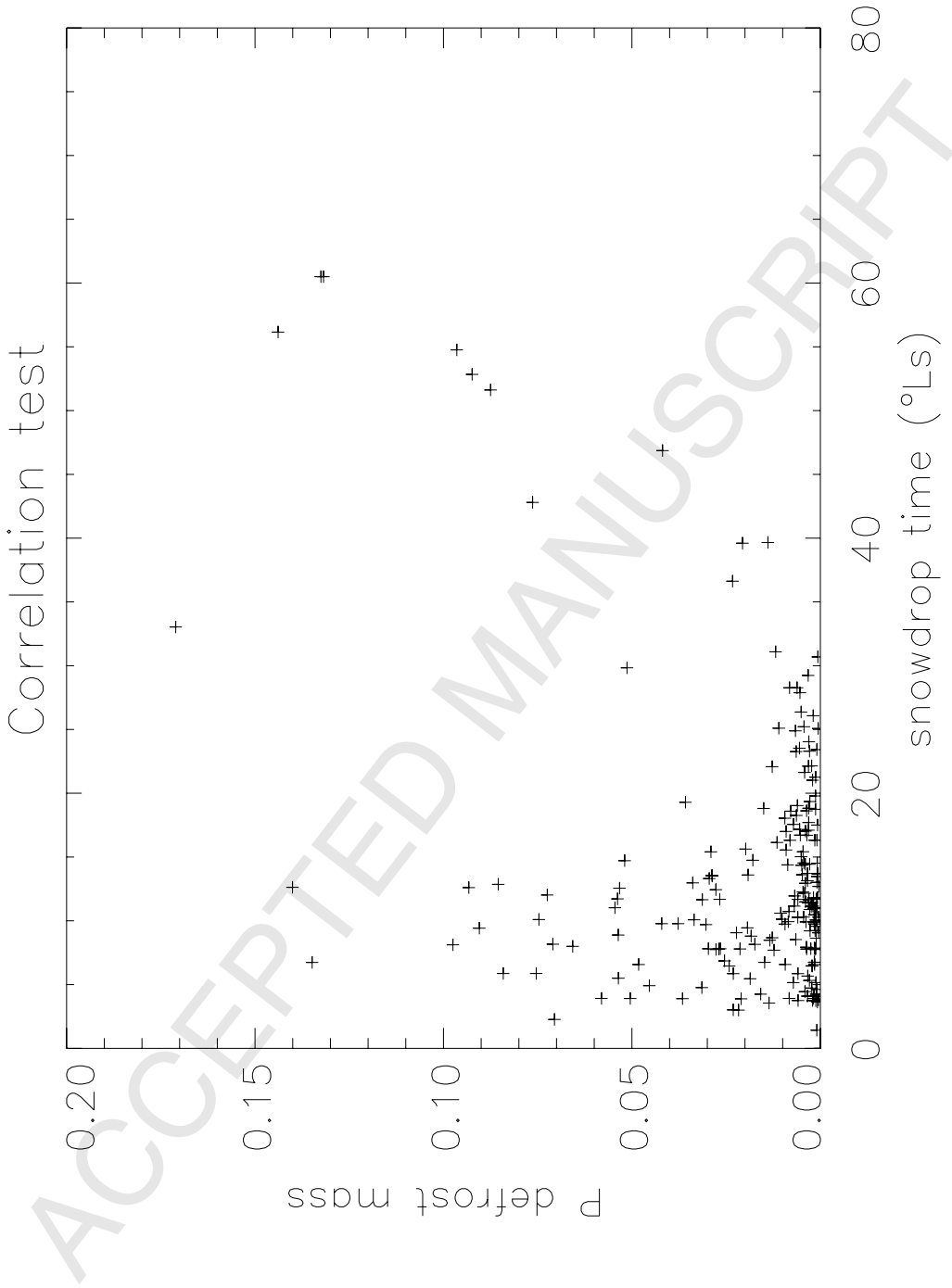

Figure 14.